Arts & Sciences Electronic Theses and Dissertations

Arts & Sciences

Winter 12-15-2014

X-Ray Polarimetry with X-Calibur

Qingzhen Guo
Washington University in St. Louis

WASHINGTON UNIVERSITY IN ST. LOUIS

Department of Physics

Dissertation Examination Committee:

Henric Krawczynski, Chair

Mark Anastasio

Thomas Bernatowicz

Ramanath Cowsik

Martin Israel

Richard Laforest

X-Ray Polarimetry with X-Calibur

by

Qingzhen Guo

A dissertation presented to the

Graduate School of Arts and Sciences

of Washington University in

partial fulfillment of the

requirements for the degree

of Doctor of Philosophy

December 2014

St. Louis, Missouri

TABLE OF CONTENTS

Page

<div align="center">LIST OF FIGURES</div>

LIST OF TABLES

ACKNOWLEDGMENTS

First of all, I am profoundly grateful to my advisor, professor Henric Krawczysnki. He is a great role model as a scientist and it is my honor to be his Ph.D. student. I am greatly impressed by his wisdom, great erudition, diligent working, thorough thinking and generosity. He helps me a lot with my research, my studies and my classes. I remember that he brought some of his children's books to me to help me improve my English when I was new here five years ago. He also recommended and lent me a lot of his astrophysics books. His encouragement and support brought me to this current step. I really appreciate his patience and generousness with all the mistakes I have made. He is always there to help me whenever is necessary.

I am very honored to work with the brilliant scientists, engineers, technicians and postdoctors in the experimental astrophysics group of Washington University. Many thanks to professors Martin Israel, Bob Binns, Jim Buckley, Matthias Beilicke,Viatcheslav (Slava) Bugayov, and also Paul Dowkontt, Garry Simburger, Marty Olevitch, Dana Braun, and Richard Bose. Extra thanks go to professor Matthias Beilicke for helping me a lot all through my 5-year Ph.D studies.

Professors Mark Anastasio, Thomas Bernatowicz, Ram Cowsik, Martin Israel and Richard Laforest are deeply appreciated too for serving on my dissertation committee. Thank you very much for your time and help.

Zhou, Kefeng Shi, Charlene Harris, Ed Harris, Yao Xie, Chuanmei Zhu, Mingyu Yang, Raymond Lai, Polina Kadatska, Erika Orban, Yuying Chen, Kun Liu, Xi Qiu, Boris Tchatalbachev, Xixi Zhang, Vicki Jameson, Zihan Xu, Brian Smith, Ke Ke, Xialing Ulrich, Bob Ulrich, Yaping Zhang, Gang Wu, Liz Kiernan, Zhongyan Li, Renyu Zhang, Sichong Zhu, Sijia Wang, Tianhui Gu,Yumei Xia et al..

A deep gratitude goes to my family: my husband, my daughter, my parents, my parents-in-law, my sisters, my brothers, and all other relatives. Their love and support is the greatest motivation to me in my Ph.D. studies. Special thanks go to my daughter Vivian who brings so much love and fun to me. Extra thanks go to my mother-in-law for helping me take care of Vivian during my Ph.D. studies.

Finally, many thanks to everyone!

Qingzhen Guo

Washington University in St. Louis

December 2014

ABSTRACT OF THE DISSERTATION

X-Ray Polarimetry with X-Calibur

by

Qingzhen Guo

Doctor of Philosophy in Physics

Washington University in St. Louis, 2014

Professor Henric Krawczynski, Chair

X-ray polarimetry is a prime tool to investigate the unexplored compact sources
and to provide crucial information that other techniques can not produce. By measur-
ing the degree and orientation of the polarization of radiation from a cosmic source,
unique inferences about the morphology and the magnetic field structure can be made.

Krawczysnki's group at Washington University is working on a uniquely sensitive
scattering polarimeter, X-Calibur, to be used in the focal plane of a focusing X-
ray telescope. The design of X-Calibur is based on Thomson/Compton/Rayleigh
scattering effects. All these scattering processes share the property that the photons
scatter preferentially to the direction perpendicular to the electric field vector. X-
Calibur consists mainly of a low-Z scintillator stick as Compton scatterer and high-Z
semiconductor CdZnTe detectors surrounding the Compton scatterer to absorb the

scattered photons. It performs X-ray polarimetry measurements in the energy range 2-75 keV when it is carried on a satellite, and in the 20-75 keV range when it is carried on a balloon. X-Calibur achieves a high detection efficiency of >80% and an averaged energy resolution (FWHM) of 3 to 5 keV over the energy band at a very low background level.

First, I report on the optimization of the scattering X-ray polarimeter X-Calibur on board InFOCμS X-ray telescope balloon flight at Fort Sumner (NM) in Fall 2014. The optimization is based on Monte Carlo simulations of polarized and unpolarized X-ray beams and the most important background components. I calculated the sensitivity of the polarimeter for the upcoming balloon flight in Fort Sumner and for additional longer balloon flights.

Additionally, I describe the optimization of the design to extend the energy range of the polarimeter towards lower energies. Such a broadband polarimeter would use LiH as the scatterer as it combines a high efficiency for scattering interactions even at <10 keV energies (as opposed to photoelectric effect absorption interactions) with a relatively high density.

Lastly, I describe the scientific potential of spaceborne observations of blazars with a first generation X-ray polarimeter mission like X-Calibur, GEMS and XIPE. I present a proposed observation program including observations strategies, sources of interest, recommended accompanying multiwavelength observations, and the observations results. The analysis uses the daily flux values of all monitored sources by the RXTE All-Sky Monitor (2-12 keV) and Swift BAT 70-month hard X-ray survey

(15-50 keV). Based on the analysis, fifteen sources are selected as target candidates for the science investigations.

1. The polarization of cosmic X-ray sources

1.1 Elementary processes producing polarized X-rays

Spectral and morphological studies of X-ray emissions play an important role in the study of astrophysical sources [1], and have led to the Nobel prize award going to Riccardo Giacconi in 2002, one of the pioneers of imaging X-ray telescopes. The fields of imaging, spectral and imaging spectropolarimetric observations are rather mature [2–7]. Largely unexplored X-ray polarimetry is a prime tool to investigate sources which are so compact that they cannot be imaged [8].

This chapter presents several motivations for using polarimetry of X-rays and γ-rays as an astrophysical tool and describes why polarimetric observations can provide unique insights into the geometries of X-ray and γ-ray emitting objects. Many of the emission mechanisms leading to the production of highly polarized X-rays and γ-rays are non-thermal and far from equilibrium, for example, highly energetic particle beams propagating through very strong magnetic fields [9]. Several mechanisms can lead to photon emission with large linear polarizations that are dependent upon the exact source geometry. Lei et al. gave a detailed review of emission mechanisms that can generate polarized X-rays and γ-rays that depend on exact source geometry

[9]. Polarization measurements can thus be used to constrain the geometry of these sources.

Electrons play a crucial role in the radiation process. Compared to heavily charged particles like protons and ions, it is much easier to accelerate electrons because they have a relatively small mass. The type of the electromagnetic radiation and its properties depend on the electron's speed. In the following sections, I will discuss several important types of radiation mechanisms and the polarization properties of the X-rays generated in these radiation processes.

1.1.1 Cyclotron emission

In cosmic settings, electromagnetic radiation is emitted by accelerated charges, and charges accelerate owing to electromagnetic forces. With a pitch angle α between the magnetic field B and the instantaneous velocity v, the motion of the electron in a uniform magnetic field is a combination of circular motion and uniform motion along B, as shown in Figure 1.1 [9, 10]. The electron is accelerated perpendicular to the vector of its velocity v.

Usually one refers to the emission of non-relativistic electron moving in magnetic field as cyclotron emission. The angular cyclotron frequency is:

$$\omega_L = \frac{eB}{m_0 c}.\tag{1.1}$$

Here e is the charge of an electron and m_0 is the rest mass of electron.
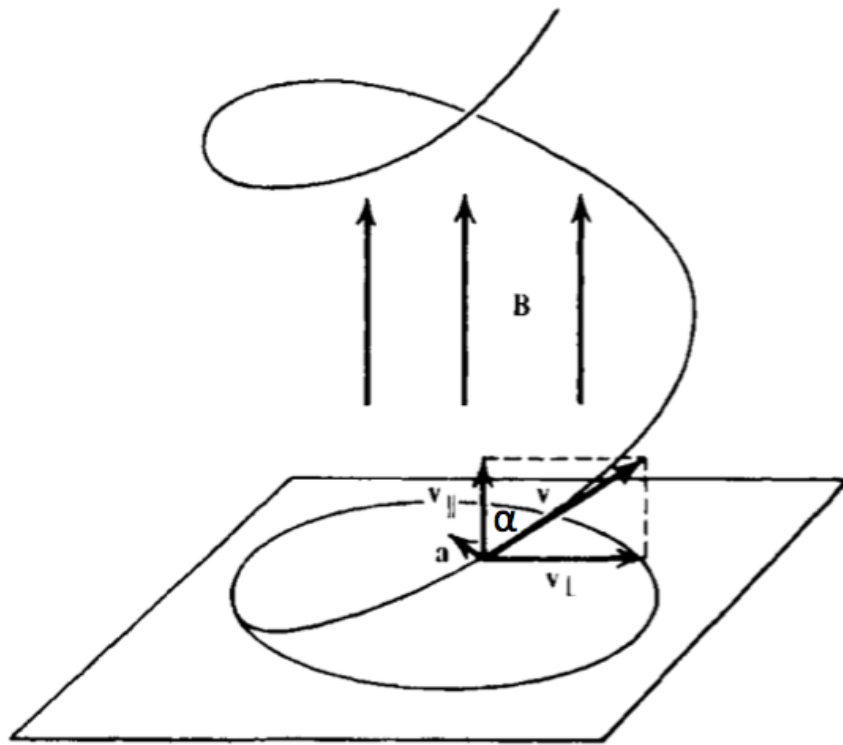
Figure 1.1. This figure illustrates the motion of an electron in a uniform magnetic field B with a pitch angle α [10].

The radiation power per unit solid angle is proportional to $sin^2\theta$:

$$\frac{dP}{d\Omega} \propto sin^2\theta \qquad (1.2)$$

while θ is the angle between the vector of the emitted photon and the acceleration vector of the electron [10]. The intensity of the radiation emission is distributed as a dipolar pattern as shown in Figure 1.2 [9, 11]. There is no radiation in the direction parallel to the acceleration vector. The intensity of the radiation is greatest in the direction perpendicular to the acceleration vector. The emitted photon is polarized with the vector of its electric field in the plane of the acceleration and velocity vectors (see Figure 1.2).

For a single non-relativistic electron in magnetic field, the total radiation power in unit erg/s is given by the following equation:

$$P_{Cyc} = 1.6 \times 10^{-15} \beta^2 B^2 sin^2\alpha. \qquad (1.3)$$

Here $\beta = v/c$, B is the magnetic induction in Gauss, and α is the pitch angle between B and v.

In most astrophysical settings, cyclotron emission is not as important as synchrotron emission (see Section 1.1.2) because the magnetic fields associated with most of the astrophysical sources are weak, between 10^{-8} and 10^{-6} G. This is because the angular cyclotron frequency (see Equ. 1.4) is very small, and the radiation power of the non-relativistic electrons is also very low. However, for astrophysical sources
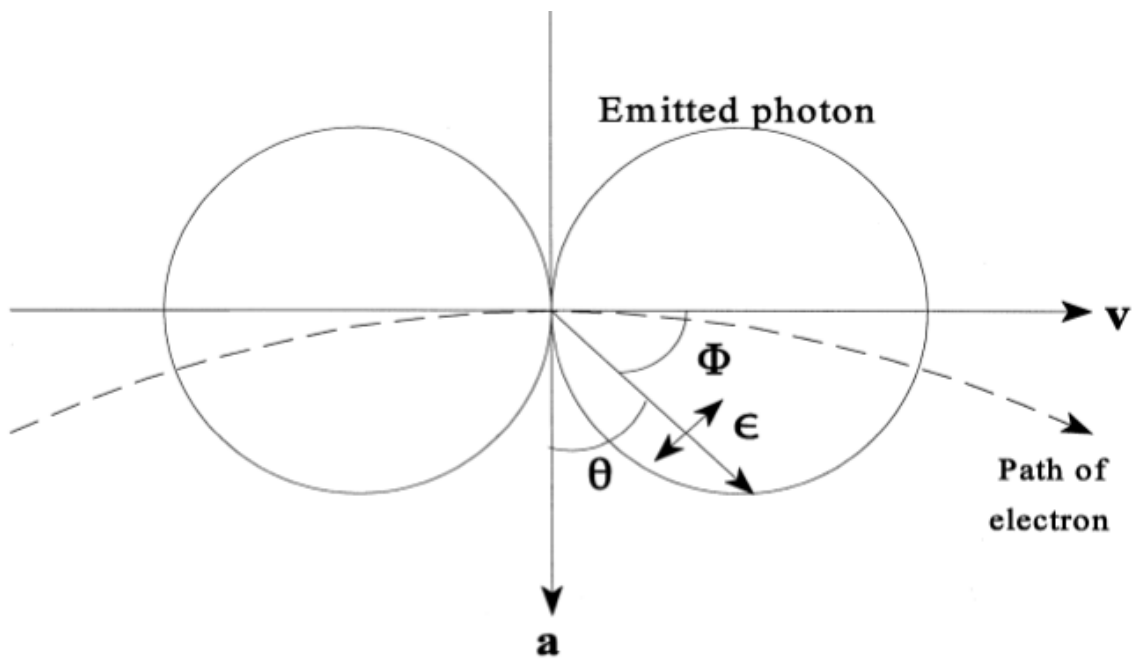
Figure 1.2. This illustration presents a polar diagram of the intensity of the radiation emitted by a non-relativistic accelerated electron [9].
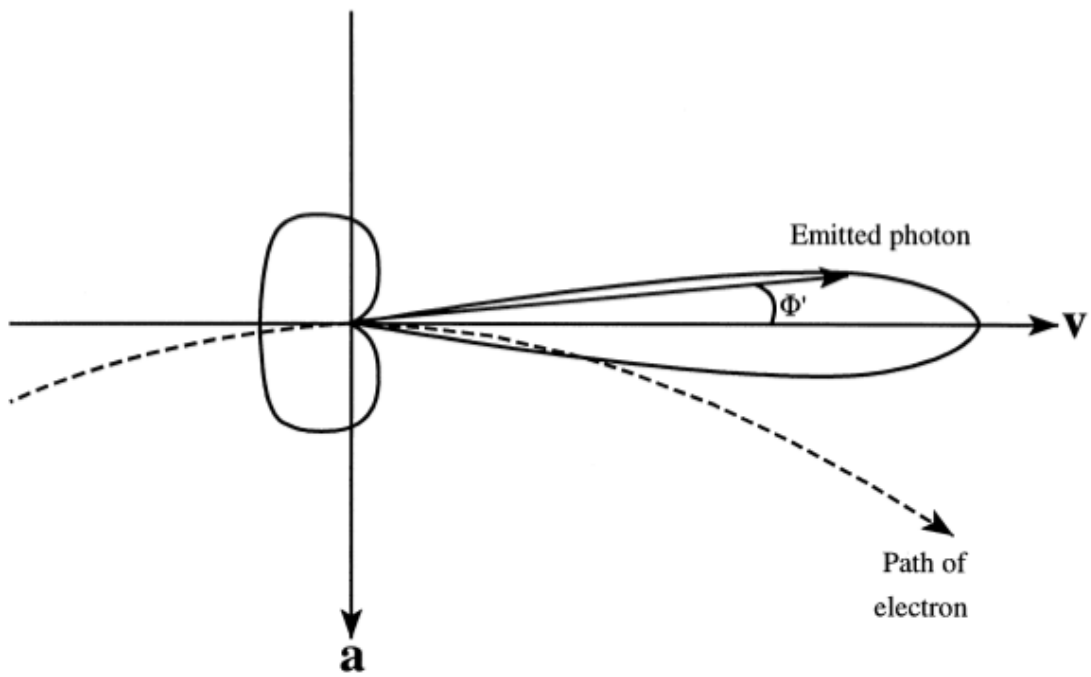
Figure 1.3. The intensity of radiation emitted by a relativistic accelerated electron is beamed in the observers frame of reference [9].

with strong magnetic fields (e.g. neutron stars) the cyclotron emission becomes very important.

1.1.2 Synchrotron emission

In magnetic field, relativistic electrons emit synchrotron emission. It is named synchrotron emission because it was first discovered in a synchrotron accelerator [12]. The angular synchrotron frequency is:

$$\omega_L = \frac{eB}{\gamma m_0 c}. \tag{1.4}$$

Here, γ is the Lorentz factor, $\gamma = (1 - \beta^2)^{-1/2}$, $\beta = v/c$, and c is the speed of light.

For a single relativistic electron in a magnetic field, the total radiation power in unit of erg/s is given by the following equation:

$$P_{Syn} = 1.6 \times 10^{-15} \beta^2 \gamma^2 B^2 sin^2 \alpha. \tag{1.5}$$

In this case, the Lorentz transformation from the inertial frame of the electron to that of the observer is important. The consequences are that the emission from relativistic charges is concentrated into the forward direction in which the particle is moving (see Figure 1.3). As the particle spirals around the magnetic field line, it emits a beam that hits the observer periodically. The Fourier transform of the emission exhibits a broad maximum at a frequency that is characteristic for the duration of the individual observed pulses. Synchrotron emission is thus inherently a broadband

emission process, in contrast to the more monoenergetic cyclotron emission. The energy spectra of the emitting electrons can often be approximated by a power-law distribution. The energy spectrum of the emitted photon will also be a power law.

Synchrotron emission can be highly polarized. The radiation from a single electron is generally elliptically polarized with a circular (linear) polarization fraction that decreases (increases) with increasing electron energy. The net polarization is calculated by the integration over all the electrons that have contributed to the total intensity. For electrons with a power-law energies distribution, $dN/dE \propto E^{-p}$, in a uniform magnetic field, the observable fraction of polarization is as follows [9, 10, 13]:

$$\Pi = \frac{p+1}{p+\frac{7}{3}}.$$

(1.6)

1.1.3 Curvature emission

Curvature radiation is a special form of synchrotron emission emitted by relativistic charged particles streaming along a curved magnetic field. It is important in rapidly rotating neutron stars and pulsars [17, 18]. At any moment, the motion of a single electron is similar to that in a uniform magnetic field. Therefore, the radiation properties of curvature emission are very similar to that of synchrotron except with some adjustments of the parameters. In the curvature radiation process, the polarization vector lies parallel to the vector of the magnetic field.

1.1.4 Bremsstrahlung radiation

In plasma, electrons and ions collide. The electrons decelerate more strongly than the ions, and convert some of their kinetic energy into emitted photons. This radiation process is called Bremsstrahlung radiation, or free free radiation. During the Bremsstrahlung radiation process, the law of conservation of energy is satisfied.

The emission of photons is likely to be perpendicular to the electron's plane of motion. The polarization vector is parallel to the direction of deceleration. Depending on the scattering angle, the polarization fraction can reach the maximum of $\sim 80\%$ [9].

1.1.5 Scattering

Photons can scatter off free or quasi-free electrons. Depending on the energy of the photon we distinguish between Thomson scattering ($E_\gamma \leq 10$ keV) and Compton scattering ($E_\gamma \geq 10$ keV). Owing to the kinematics of the interaction, photons lose negligible energy in the Thomson scattering process. When the photon energies is a significant fraction of the electron rest mass (i.e. the Compton scattering regime), the photons can lose a large fraction of their energy to the recoiling electron. Figure 1.4 shows a schematic view of the Compton scattering process off a valence electron of an atom. The photon is scattered with some reduction in energy and momentum. When a photon scatters off an energetic electron and gains energy, we call the process inverse Compton scattering. Inverse Compton scattering is very important in studies
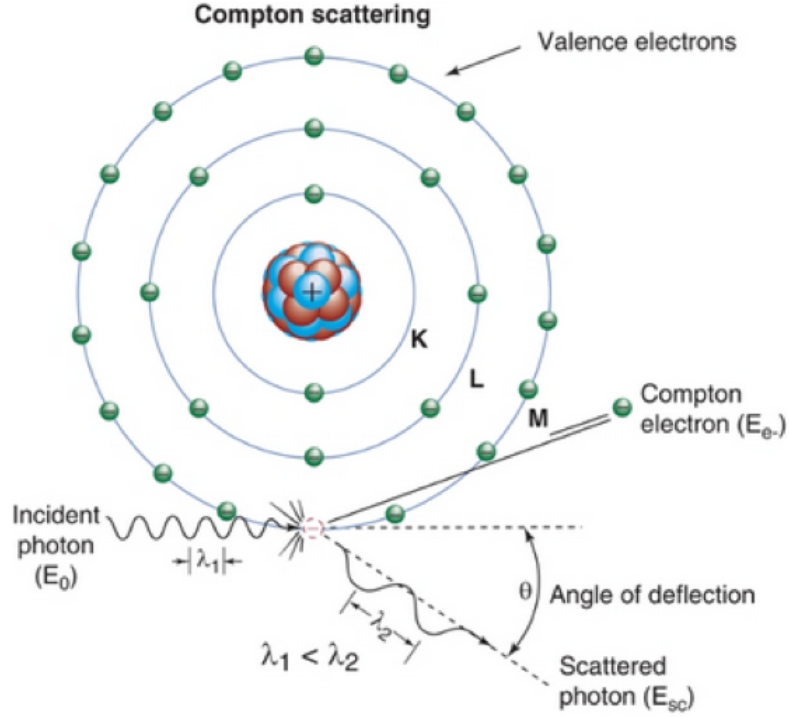
Figure 1.4. Schematic diagram of the Compton scattering process. The incident photon at energy E_0 interacts with a valence shell electron leading to the energy of the photon being reduced to E_{sc} and an ejected Compton electron at energy E_{e-} [19].

of mechanisms producing X-rays and γ-rays in astrophysics. The high-energy emission from blazars for example is thought to originate as inverse Compton emission.

The cross section of Thomson and Compton scatterings is the Klein-Nishina cross section [20]:

$$\frac{d\sigma}{d\Omega} = \frac{r_0^2}{2} \frac{k_1^2}{k_0^2} \left[\frac{k_0}{k_1} + \frac{k_1}{k_0} - 2sin^2(\theta)cos^2(\eta) \right] \qquad (1.7)$$

where r_0 refers to the classical electron radius, while k_0 refers to the wave vectors before scattering and k_1 refers to that after scattering. θ is the scattering angle between k_0 and k_1, and η is the angle between the scattering plane and the electric vector of the incident photon. k_1 can be computed as function of k_0 and θ by the Compton scattering equation as following:

$$\Delta\lambda = \frac{h}{m_e c}(1 - cos(\theta)). \tag{1.8}$$

The degree of linear polarization of the scattered photons is given by

$$\Pi_P = 2\frac{1 - sin^2(\theta)cos^2(\eta)}{\frac{k_0}{k_1} + \frac{k_1}{k_0} - 2sin(\theta)cos(\eta)}. \tag{1.9}$$

Both Compton and inverse Compton scattering are able to generate photons with a non-zero polarization fraction from unpolarized beams. An X-ray or γ-ray beam may undergo multiple scatterings. In this case, scattering is also able to depolarize an originally polarized beam, which leads to the reduction of the degree of linear polarization [9]. The fraction of linear polarization from Compton or inverse Compton scattering depends on the relative orientation of the electric field of the incoming photons and their scattering planes. Scattered beam will be composed of polarized components from all incident directions for an isotropic distribution of incident photons. These components can cancel each other and leave a completely non-polarized beam [9].

1.1.6 Other effects affecting the polarization

Radiation can become polarized and/or depolarized when interacting with a magnetized plasma. In magnetars, only one polarization direction can propagate, leading to a polarization of the thermal emission from the magnetar surface [22]. In most objects, the polarization can change owing to energy dependent Faraday rotation when the photons traverse a magnetized plasma.

1.2 Cosmic sources of polarized X-rays

1.2.1 Black holes

The two most common types of black holes are stellar mass black holes (the endpoints of the evolution of massive stars) with typical masses of between ∼3 and 20 solar masses, and supermassive black holes that are located at the centers of galaxies with typical masses of several million to several billion solar masses. Both types of black holes can be copious emitters of X-rays when they accrete matter through an accretion disk. Stellar mass black hole can accrete matter from a companion. Supermasive black holes accrete matter from the interstellar medium. The accretion disks of stellar mass black holes thermally emit X-rays as the accretion disk material heats up owing to viscous dissipation inside the accretion disk. The accretion disks of supermassive black holes thermally emit optical/UV radiation and emit X-rays owing to hot electrons in (most likely) magnetically heated accretion disk coronas.

There are a few unknown topics of black holes of great interest, for example, the geometry and dynamics of the X-ray source regions. X-ray observations of black holes can also be used to test the predictions of the theory of General Relativity in regimes of strong-field gravities.

Stark & Connors [23–25] showed that polarization fraction which is dependent on energy would be generated by gravitational lensing, relativistic aberration, beaming and so on. Schnittman & Krolik [26, 27] calculated the expected polarization signature. Photon at higher energy is generated closer to the black hole than that at lower energy. Owing to the strong spacetime curvature around the black hole, these high energy photons are more likely to be scattered as they can return to the accretion disk [26, 27].

1.2.2 Neutron stars, magnetars and pulsars

Neutron stars provide a chance to study the behavior of matter and radiation at high density and under the influence of strong magnetic fields. Magnetic fields are so strong in these objects that intrinsically polarized emission is a virtual certainty, and the observed polarization is thus a measure of the geometrical arrangement of the field and emitting gas. Fundamental physics associated with the behavior of radiation in strong magnetic fields is expected to yield a characteristic signature in the polarized spectrum of the most extreme class of magnetized objects.

In pulsar magnetospheres, the presence of high-energy particles can lead to emission of curvature and synchrotron radiation. Solely based on the observed photon en-

ergy spectrum, it is difficult to distinguish the curvature radiation from synchrotron radiation. Dyks [29] illustrated some models of the phase dependence of the X-ray and γ-ray polarization signatures in pulsars. Given more compact emission regions at high energies, a higher polarization degree of hard X-ray is potentially shown by these objects [31].

1.2.3 Jets in AGNs

The collimated outflows (jets) from Active Galactic Nucleis (AGNs) are strong emitters of X-ray emission. One would like to use the emission to study the structure and make up of the jets, and ultimately to learn how jets are launched and accelerated, and how they maintain their collimation. Polarization provides a way to probe the structures of the magnetic fields inside jets. Particles moving through a standing shock accelerated in a helical field leads to synchrotron emissions and polarization direction swings [47]. At optical wavelengths, an event like this has been observed from BL Lac objects [103]. The electron population can produce photon emissions extending from optical to the γ-ray range by inverse Compton scattering a photon field.

Compared to synchrotron self-Compton models, a higher fraction of polarization at high energies is predicted in hadronic jet emission models for low-synchrotron-peaked blazars as the X-ray emission could originate in this case as synchrotron emission of high-energy protons [38].

2. X-ray and γ-ray polarimeters and their results to date

So far NASA has launched just one dedicated X-ray polarimetry experiment and there is just one unambiguous astrophysical result available at the time of writing this thesis due to the difficulty of measuring the polarization of X-rays. Measuring the polarization properties of X-rays requires many more photons than imaging or spectroscopic studies.

In this chapter, I will give a brief review of X-ray polarimetry missions to date and the upcoming X-ray polarimetry experiments besides X-Calibur.

2.1 X-ray polarimetry missions to date

2.1.1 OSO-8

The 8th Orbiting Solar Observatory (OSO-8) with a focusing Bragg crystal reflectometer on board was launched in June 1975. OSO-8 was the first high-sensitivity solar polarimetry satellite mission [49]. The sun was its primary target. Four instruments carried on OSO-8 were dedicated to observations of other celestial X-ray sources. OSO-8 mission terminated operations on October 1st in 1978.

The Bragg reflectometer was used to measure the polarization of the X-rays from the Crab Nebula and pulsar at 2.6 keV and 5.2 keV [48]. The X-ray polarization

degree at 2.6 keV of Crab nebula was measured to be (19.2±1.0)%, and the position angle was (156.4±1.4)°. The corresponding measured values were (19.5± 2.8)% and (152.6±4.0)° at 5.2 keV [49]. These results are consistent with radiation arising from synchrotron processes [48]. Observations of Cygnus X-1 provided weak evidence for a polarized signal, indicating a polarization fraction of a few percent. The polarization fraction detected by OSO-8 was (2.44±0.85)% at a direction of (162±10)° [49].

The low efficiency of the OSO-8 polarimeter (arising form the narrow bandpass of the Bragg reflectometer) severely limited the observing program, and sensitivities to polarization degrees below 5% were achieved only for 3 sources beyond the Crab nebula detection [51]. The polarimeter was not able to perform accurate measurements of the phase resolved polarization properties of the Crab pulsar owing to the limited photon statistics [49].

2.1.2 INTEGRAL

The INTErnational Gamma-Ray Astrophysics Laboratory (INTEGRAL) was a satellite mission launched on October 17, 2002. INTEGRAL carried two γ-ray telescopes [53]. The spectrometer SPI (SPectrometer on INTEGRAL, Germanium array) [54] was designed for line spectroscopy measurements from 20 keV to 8 MeV of the γ-ray. The Imager IBIS (Imager on Board the Integral Satellite, CdTe array) [56] was designed for imaging measurements from 15 keV to 10 MeV. There were also two monitors on board INTEGRAL, JEM-X and OMC. JEM-X [55] measured the X-ray in the energy range from 3 to 35 keV [53].

INTEGRAL performed polarization studies of the Crab Nebula and Cygnus X-1 with the goal of constraining the polarization properties of their hard X-ray emission. Dean et al. reported a polarization of the 100 keV-1 MeV emission of $46\% \pm 10\%$ with a position angle of $(123.0\pm11)°$ based on the 2003 to 2006 SPI data [61]. The IBIS was used to study the Crab in the energy range from 200 to 800 keV [31]. There were not any significant polarization reports for either pulsar peak. A polarization degree $>72\%$ with the position angle at $(120.6\pm8.5)°$ was reported in the off-pulse region. No polarization was detected for the phase bins corresponding to the pulsar pulses. The results were modified to $> 88\%$ and $(122.0\pm7.7)°$ if the bridge region was also taken into account. Cygnus X-1 was also studied with the IBIS instruments. A polarization fraction of $(67\pm30)\%$ with a position angle of $(140\pm15)°$ was found between 250 and 400 keV. Data from 200 keV to 1 MeV taken by IBIS were analyzed and the results indicated a higher polarization degree [31]. The large (mostly systematic) error on the polarization fraction highlights the difficulty to measure polarization properties with an instrument that was not designed for this purpose.

2.1.3 IKAROS

The Interplanetary Kite-craft Accelerated by Radiation Of the Sun mission (IKAROS) was launched with the wide field-of-view Gamma-ray Burst Polarimeter (GAP) with a sensitive energy band from 50 to 300 keV. The GAP measured the polarization of X-rays based on measuring the azimuthal distribution of Compton scattered photons. A dodecagon plastic scintillator, located at the center of the detector assembly, serves

as Compton scatterer. It is read out by a PMT (photomultiplier tube). The scatterer is surrounded by 12 CsI scintillators with PMT readout [57].

The GAP observations revealed three GRB polarization detections. The GRBs GRB100826A, GRB110301A and GRB110721A were found to be polarized on confidence levels of 99.9%(3.5σ), (70±22)% and (84$^{+16}_{-28}$)% , respectively [62,63]. The data indicates polarization fractions of between 27% and 84%.

2.2 Other upcoming X-ray polarimetry experiments

2.2.1 ASTRO-H

The Japanese led ASTRO-H mission (scheduled to launch in 2015/2016) carries four focusing X-ray and γ-ray telescopes [58]. Two of them are Soft X-ray Telescopes (SXTs), operated from 0.3 keV to 12 keV [58]. A micro calorimeter spectrometer array and X-ray CCD array are located in the focal plane of the two SXTs, respectively [58].

There are two more Hard X-ray Telescopes (HXTs) which will operate from 5 keV to 80 keV. The Hard X-ray Imager carried on the HXT consists of Si and CdTe cross strips detectors. The Soft γ-ray Detector carried on HXT, called Si/CdTe Compton Camera, consists of Si and CdTe pixelized detectors, and a collimator [64]. The Soft γ-ray Detector can do Compton polarimetry at >50 keV energies for sources that are brighter than several tens of mCrabs. The spectropolarimetric observations with

ASTRO-H may also be deteriorated by similarly large systematic errors as polarimetry is not the primary focus of the experiment.

2.2.2 PoGOLite

The light-weight Polarized γ-ray Observer (PoGOLite) [65] is a balloon experiment designed for the polarization measurements and studies of hard X-rays and soft γ-rays emission between 25 keV and 100 keV from compact astrophysical sources [66]. PoGOLite is made of 217 Phoswich Detector Cells (PDCs), which are plastic scintillator rods, with each rod being surrounded by BGO [65]. Plastic scintillators are used for both the Compton scattering and the photoabsorption process to maximize the effective area at 20-100 keV.

The Crab Pulsar and Cygnus X-1 are the primary target sources for the first balloon flights with PoGOLite. The polarization direction and fraction of incident photons are determined by events detected in coincidence in two or more detectors. These events are largely caused by a Compton scattering in one detector element followed by a photoelectric effect absorption process in another scattering element. Other event types include multiple Compton scattering events as well as chance coincidences. The MDP (minimum detectable polarization) is estimated to be about 10% for a 200 mCrab Crab-like source for a single PoGOLite balloon flight [65].

2.2.3 ACT

The Advanced Compton Telescope (ACT) [67] is a concept for a next-generation Compton telescope. The ACT is being developed based on the technique of imaging used in COMPTEL on board CGRO and improved with advanced technologies of detector and integrated readout electronics. The ACT would use an array of 3-D position sensitive Ge detectors [67].

ACT would be able to measure a broad spectral band from 0.2 to 10 MeV for Compton imaging, from 10 keV to 10 MeV for spectroscopy with an accurate timing of $1\mu s$ and novel capabilities for X-ray and γ-ray polarization measurements [67].

2.2.4 GEMS

The Gravity and Extreme Magnetism Small explorer (GEMS) was a proposed X-ray polarimetry mission. GEMS was designed to use two X-ray telescopes, each with focusing X-ray mirrors and a soft X-ray polarimeter. Each soft X-ray polarimeter would be made of three time projection chambers which would be used to track the photoelectrons ejected in photoelectric effect interactions.

Baumgartnera [69] estimated that the modulation factor μ_{100} of GEMS increases from zero to 0.6 from 2 to 10 keV. It would have been able to perform measurements of the polarization of 2-10 keV, but have the best sensitivity at 2-5 keV [107].

GEMS was an approved NASA Small Explorer (SMEX) mission with a projected 2014 launch. The program was terminated due to schedule delays and financial problems in 2012.

2.2.5   XIPE

The X-ray Imaging Polarimetry Explorer (XIPE) was a small spectral and imaging polarimetry mission concept that was proposed as a small ESA mission in 2012 [70]. Unfortunately the proposal was not selected.

XIPE was designed to use existing X-ray optics with demonstrated properties. XIPE would use a polarimeter similar to the one used by GEMS. However, the readout would be different. Wheras GEMS combines readout strips with drift time measurements, XIPE would use a proportional chamber with a 2-D pixel readout. For a faint 1 mCrab source, was estimated to be around 14% for an observation time of 10^5 s in the energy range 2-10 keV [70].

3. Optimization of the design of the hard X-ray polarimeter X-Calibur

3.1 Overview of X-Calibur

Our Washington University group is developing the scattering polarimeter, X-Calibur. In this chapter, I report on the optimization of X-Calibur when used in the focal plane of the InFOCμS X-ray telescope. We plan to fly the experiment in Fall 2014 from Fort Sumner (NM) on a high-altitude (40 km) balloon flight. About 70% of this chapter has been published as a refereed journal paper [71]. I am the leading author of that paper. I wrote 80% of the text of the paper (my advisor wrote the rest), and contributed almost all the analysis results presented in the paper. David Fleming (a undergraduate researcher) contributed Figure 3.4 to the paper.

X-Calibur is a polarimeter for the focal plane of an imaging mirror assembly similar to the ones used in the HERO [74], HEFT [75], InFOCμS [73] and NuSTAR [75,76] experiments. X-Calibur uses low-Z and high-Z materials to scatter and absorb incident X-ray photons, respectively. The design aims at achieving the best possible polarization sensitivity in the hard X-ray (20-75 keV) band. Three properties make X-Calibur more sensitive than the competing hard X-ray polarimeters designs: high dectection efficiency, low background and reduced systematic uncertainties. Most

Figure 3.1. InFOCμS balloon gondola. The X-Calibur polarimeter will be located in the focal plane of the Wolter X-ray mirror (40 cm diameter) with a focal length of 8 m [72, 73].

hard X-ray Compton polarimeters (e.g. POGO [77], GRAPE [78, 79], and HXPOL [80]) use only 10-20% of the photons that imping on the detector assembly while the detector configuration of X-Calibur can achieve >80% detection efficiencies over most of its energy range. X-Calibur achieves lower background levels than other hard X-ray polarimeters that do not use focusing optics and use massive detector elements to collect the photons. The Grazing incidence mirrors change the polarization properties of X-ray by less than 1% [81, 82]. Ring bearing is designed for X-Calibur to reduce and minimize the systematic uncertainties. X-Calibur is designed to spin around the optical axis during the observations which will be used to distinguish ϕ-modulations caused by detector effects from that caused by the polarization of the observed source.

The X-Calibur design trades a high detection efficiency for imaging capabilities. This is well justified given that the most interesting targets for X-Calibur (accreting black holes and neutron stars) are too small to be spatially resolved by current technology. Below, I report on the sensitivity of X-Calibur when flown with different mirror assemblies on balloon-borne missions. NASA approved a one-day balloon flight of X-Calibur in the focal plane of the InFOCμS X-ray telescope [73] from Fort Sumner (NM, 34.47°N, 104.24°W) in Fall 2014 and a >20 day long duration balloon flight from McMurdo (Antarctic) in 2015. The InFOCμS telescope will be equipped with a 40 cm diameter 8 m focal length Wolter type Al mirror assembly developed at Nagoya University, as shown in Figure 3.1. The mirror was flown already on the 2001 and 2004 InFOCμS balloon flights and comprises 255 double reflection shells, each made of 0.17 mm thick Al-foils with a multilayer coating for a broad energy range, as

Figure 3.2. The InFOCμS Al-mirror assembly. It comprises 255 double reflection shells, each made of 0.17 mm thick Al-foils with a multilayer coating for a broad energy range [72, 73].

shown in Figure 3.2. The effective area of the mirror assembly is shown in the Figure 3.6.

In this chapter, I present results from Monte Carlo studies of the polarimetric performance of X-Calibur and the optimization of the design based on the simulations.

3.2 General considerations

In general terms, a scattering polarimeter like X-Calibur uses the fact that X-rays preferentially Raleigh, Thomson, or Compton scatter perpendicular to the orientation of their electric field vectors. The angular dependence of the scattering processes is described by the Klein-Nishina cross section as Equ. 1.7. If one accumulates many events from a linearly polarized beam and determines the azimuthal scattering angle, the distribution will reveal a sinusoidal modulation with a 180° periodicity with an amplitude and phase depending on the polarization degree and direction, respectively. An important parameter describing a polarimeter is the amplitude of the azimuthal scattering angle distribution for a 100% linearly polarized signal. This amplitude is known as the modulation factor, μ, and is defined as:

$$\mu = \frac{C_{max} - C_{min}}{C_{max} + C_{min}}, \tag{3.1}$$

where C_{max}, C_{min} refer to the maximum and minimum numbers of counts in the azimuthal scattering angle histogram. The performance of a polarimeter can be characterized by the Minimum Detectable Polarization (MDP) [83]. The MDP is

the minimum degree of linear polarization which can be detected with a statistical confidence of 99% in a given observation time T:

$$MDP = \frac{4.29}{\mu R_{src}} \sqrt{\frac{R_{src} + R_{bg}}{T}}, \tag{3.2}$$

Here, R_{src} and R_{bg} are the source and background rates of events entering the analysis, and T is the integration time.

3.3 The X-Calibur design

X-Calibur uses a low-Z scattering stick to maximize the probability of a first Compton interaction. A high-Z Cadmium Zinc Telluride (CZT) assembly is used to absorb the scattered X-rays in photoelectric effect interactions, see Figure 3.3. Owing to the properties of the Klein-Nishina scattering cross section, the azimuthal scattering angle distribution peaks at angles $\pm 90°$ from the preferred orientation of the electric field vector.

The low-Z/high-Z combination leads to a high fraction of unambiguously detected Compton events and suppresses the detection of elastically scattered neutrons that can mimic Compton events. The first X-Calibur flight will use a scintillator as the scattering stick. The scintillator is triggered when sufficient energy is deposited and read out by a PMT, allowing us to look for coincidences in the scintillator and CZT detectors and to get a better understanding of the background level. I will use the data gathered during the flight to perform detailed comparisons between the simulated
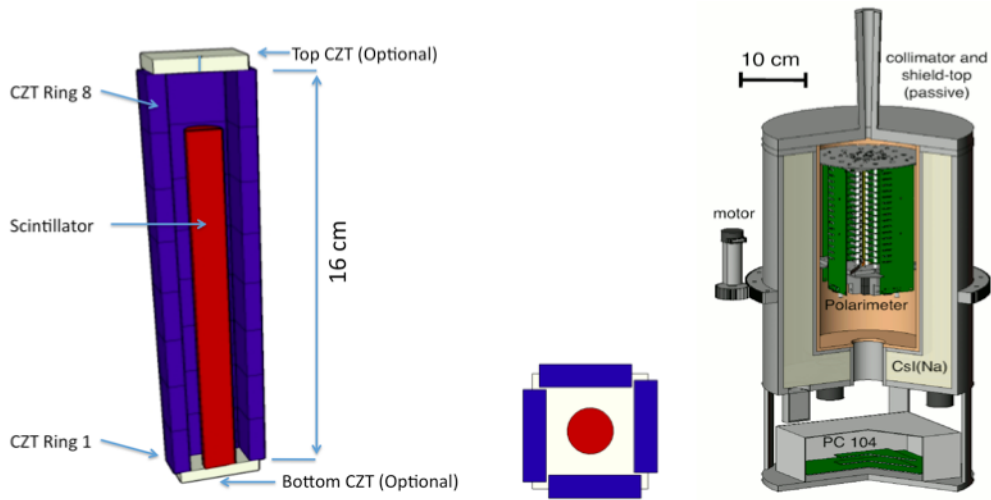
Figure 3.3. Left and center panels: conceptual design of the X-Calibur detector assembly consisting of a scattering slab (red) surrounded by absorbing CZT detectors (blue and white). The scattering slab is aligned with the optical axis of an X-ray mirror (not shown here). A large fraction of the Compton scattered photons are subsequently photo-absorbed in the high-Z CZT detectors. The distribution of the azimuthal scattering angles constrains the linear polarization of the incoming radiation. In the left panel, the white rectangles at the top (front-side, with a cylindrical bore in the center) and bottom (rear end) of the detector assembly show optional additional CZT detectors. The right panel shows the polarimeter with the readout electronics inside a fully active CsI shield which can be rotated around the optical axis.

and measured energy spectra in the CZT detectors for ON (source + background) and OFF (background only) observations. Simulated and observed background data will test the predictive power of our background model by plotting the simulated and measured CZT energy spectra: (i) for all events detected in the CZT detectors, (ii) for all events detected in the CZT detectors with and without a trigger in the scintillator slab, (iii) for all events detected in the CZT detectors with and without a shield veto, and (iv) for all events detected in the CZT detectors with and without a trigger in the scintillator slab, and for both event classes with and without a shield veto.

The length of the scintillator of X-Calibur is 14 cm. It was chosen to yield a Compton scattering probability of >90% for 75 keV photons. We performed a dedicated Monte Carlo study to optimize the diameter d of the scattering slab, accounting for the point spread function of the X-ray mirror, the defocus of the X-ray beam away from the focal point, and alignment errors (see Table 3.1). Figure 3.4 shows the Figure of Merit (FoM) as function of d. The FoM is chosen to be proportional to the modulation factor and the square root of the detection efficiency (the fraction of incident photons being scattered and reaching the CZT detectors). In the signal-dominated regime, this FoM will be inversely proportional to the MDP. A thicker scattering stick catches a higher fraction of photons and thus leads to a higher detection efficiency. I infer the azimuthal scattering angle from the position of the triggered CZT pixel assuming that the X-ray is scattered at the optical axis. For a thicker scattering stick the spatial uncertainty of the scattering location leads to larger errors in the inferred azimuthal scattering angle. As a consequence, the modulation factor decreases. Fig-
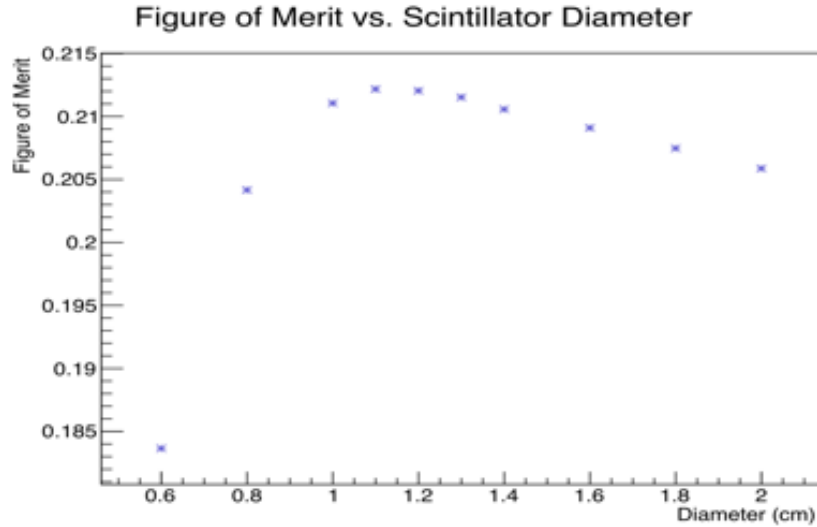
Figure 3.4. Figure of Merit values plotted vs. Scintillator Diameter prepared by David Fleming. The peak is at diameter around 1.1 cm.

ure 3.4 shows that the FoM exhibits a broad maximum for diameters between 1 cm and 1.3 cm. For our simulations described below, I assume a diameter of 1 cm.

The CZT detector confiuration is made of 32 detector units (each $2 \times 2 \times 0.2$ mm^3, more units for longer scattering sticks) with a monolithic cathode oriented towards the inside of the assembly and 8×8 anode pixels each (2.5 mm pitch) oriented towards the outside. The length of the CZT assembly is longer than the scattering stick to catch a high fraction of the scattered X-rays. In the following I assume that the CZT detectors will operate at an energy threshold of 15 keV. Such a threshold is sufficiently low for a balloon flight, as < 20 keV X-rays are almost completely absorbed in the atmosphere. For a satellite borne experiment, one would like to go to a lower energy threshold of about ∼1-2 keV. As mentioned above, I infer the azimuthal scattering angle from the position of the CZT pixel with the highest signal assuming that all

31

photons scatter at the optical axis. The residual atmosphere at balloon altitudes (2.9 g cm^{-2}) absorbs X-rays below 20 keV and the X-Calibur mirror is limited to $\leqslant$ 75 keV energies. Below I will thus plot our results only in the 20-75 keV energy range. The degree of linear polarization can be measured based on events with (or without) a trigger of the PMT reading out the scintillator stick. The events with a scintillator hit have a somewhat lower level of background contamination. In X-Calibur, there is no crosstalk between the low-Z Compton scatterer and the high-Z photoelectric-effect absorber as these two detector elements are well separated from each other. Some of the alternative Compton polarimeter designs suffer from optical and/or electronic crosstalk that can lead to the misclassification of background events as Compton-events. The polarimeter and the front-end readout electronics will be located inside an active CsI (Na) anti-coincidence shield with a passive top (see Figure 3.3) to suppress charged and neutral particle backgrounds. In the simulations, I assume the active shield is 5 cm thick and the passive shield is 2 cm thick. The active shield is read out by 4 PMTs with a high quantum efficiency super-bi-alkali photo cathodes placed at the rear end of the shield. The PMT trigger information allows effectively rejecting background from signal events.

3.4 Simulations

This section describes the simulations for the optimization of the X-Calibur design. For this purpose, I simulated polarized and unpolarized X-ray beams and the

Table 3.1

Budget of errors important for the optimization of the thickness of the scattering slab for a one-day balloon flight of X-Calibur on InFOCμS [73].

Error Source	Error [arcmin]	Error [mm]
PSF 75% Cont. Radius	2	4.6
Max. Defocus	<0.85	<2
Max. Pointing Error	<1	<2.3
Max. Align. Error	<0.85	<2
Total	<4.9	<10.6

most important background sources. The simulations account for the atmospheric absorption at float altitude (130,000 feet) and for the mirror throughput.

3.4.1 Simulation details

Our Monte Carlo study uses the Geant4 simulation package [84] and a detector simulation code. I used the GEANT4 package with the Livermore Low-Energy Electromagnetic Models [85] to simulate 2 million polarized and 2 million unpolarized photons. Photons with energies between 20 keV and 75 keV were generated according to the Crab spectrum as measured with the Swift Burst Alert Telescope (BAT) telescope [86]:

$$\frac{dN}{dE} = 10.17 \left(\frac{E}{1keV} \right)^{-2.15} ph\, cm^{-2} s^{-1} keV^{-1}, \tag{3.3}$$

I account for atmospheric absorption at a floaing altitude of 130, 000 feet using the NIST XCOM attenuation coefficients for an atmospheric depth of 2.9 g cm^{-2} [87]. The simulations assume observations at a zenith angle of 10°. Figure 3.5 shows the atmospheric transmissivity. It increases rapidly from 0.1 to 0.6 in the 20-60 keV range. Figure 3.6 shows the effective area of the Nagoya University Al mirror as function of the photon energy. The throughput is 95 cm^2, 60 cm^2 and 40 cm^2 at 20 keV, 30 keV and 40 keV respectively.

The incident photons and their secondaries are tracked through the detector volumes recording interaction locations and energy depositions occurring along the way.
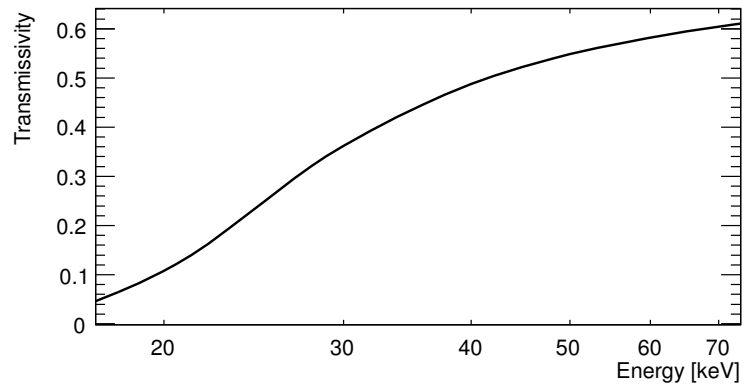
Figure 3.5. The X-ray transmissivity at a floating altitude of 130,000 feet calculated with the NIST XCOM attenuation coefficients [87] for an atmospheric depth of 2.9 g cm^{-2}.
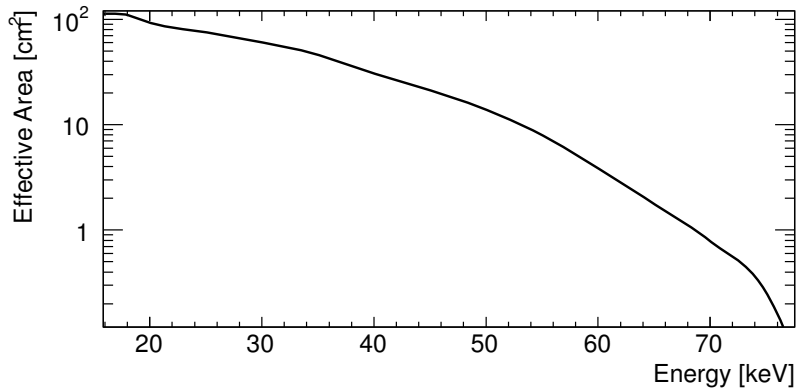
Figure 3.6. The effective area as function of the photon energy of the mirror that will be used in the first InFOCμS balloon flight planned for 2014.

The detector simulation code determines the energy deposited in the pixels of individual detectors, and generates a signal if the energy exceeds the trigger threshold. If an event triggers more than one detector element, all the energy detected in adjacent detector elements is summed together with the highest energy deposited. I use the position information of highest energy deposited in the analysis.

3.4.2 Background simulations

In this subsection, I report on background simulations. I simulated the most important backgrounds such as the Cosmic X-ray Background (CXB) [88], secondary γ-rays (upward and downward components), cosmic ray protons and electrons (of primary and secondary origin, the primaries move downwards, the secondaries move upward and downward) [89] with the MEGALIB software package [90]. I scaled these
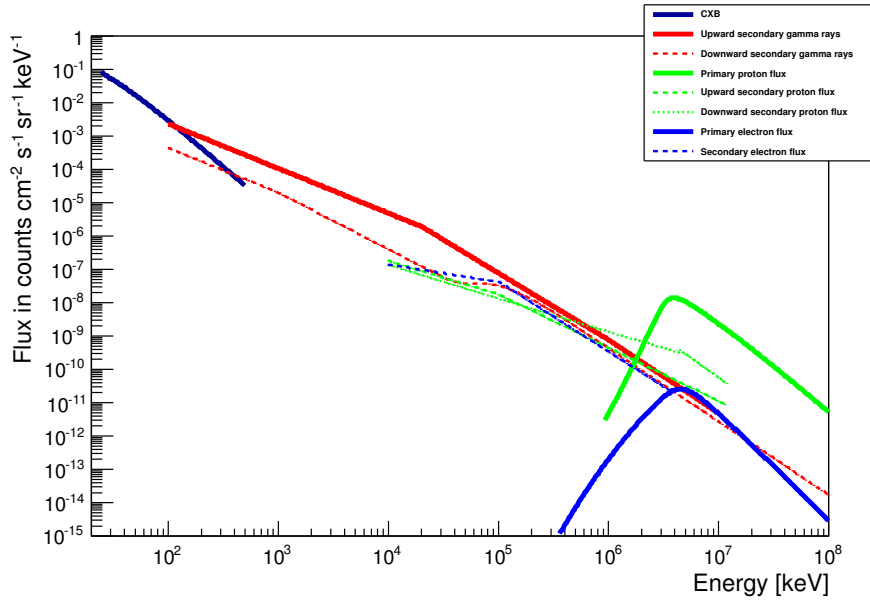
Figure 3.7. This figure shows the energy spectra of the simulated background sources. The CXB (black curve) is from M. Ajello et al. [88], and the red solid curve represents upward secondary γ-rays [89]. The red dashed curve represents downward secondary γ-rays [89]. The green solid curve is the primary proton flux [89], and the green dashed curve is the secondary proton flux [89]. The blue solid line is the primary electron flux [89] and the blue dashed line is the secondary electron flux [89]

background models taking the altitude, latitude, the effect of solar activity and earth magnetism on primary partile fluxes in Fort Sumner in fall 2014 into account. The neutron background was not modeled since the detailed studies of Parsons et al. [91] showed that neutrons do not contribute substantially to the background in CZT detectors [91] in a balloon flight. Neutrons lead to activation which is a concern for a satellite [92]. The models cover the entire solid angle (4π sr) and the energy range between 20 keV and 100 GeV. In our background simulations, the incident particles were generated on a spherical surface of 46 cm radius surrounding the detector model.

Figure 3.7 shows the background input spectra used in the simulations. Below a few hundred keV, the incident background is dominated by the CXB for all directions not shielded by the Earth. From 200 keV to ∼400 MeV, the upward-moving secondary γ-rays resulting from cosmic ray interactions in the atmosphere dominate the background. Above 10 GeV, cosmic ray (CR) protons are the main contributors to the background. Different shield configurations and shield thicknesses were simulated to optimize the shield design. I compared the background level for different shield designs, i.e. fully active shields with wall thicknesses between 2 cm and 10 cm and active/passive shield combinations.

The configuration shown in the right panel of Figure 3.3 represents a compromise, balancing the background rejection power with the mass and complexity of the shield. The shield combines a 5 cm active portion with a 2 cm thick passive Pb-cover and a Pb-collimator.

3.5 Expected performance

3.5.1 Azimuthal scattering distributions

The left panel of Figure 3.8 shows exemplary azimuthal scattering distributions for unpolarized and polarized incident X-ray beams before correction for non-uniformities. The results correspond to 5.6 hours of on-source observations of the Crab pulsar and nebula during a one-day balloon flight of the experiment from Fort Sumner using the Nagoya University Al mirror. Even for an unpolarized incident X-ray beam, the ϕ-
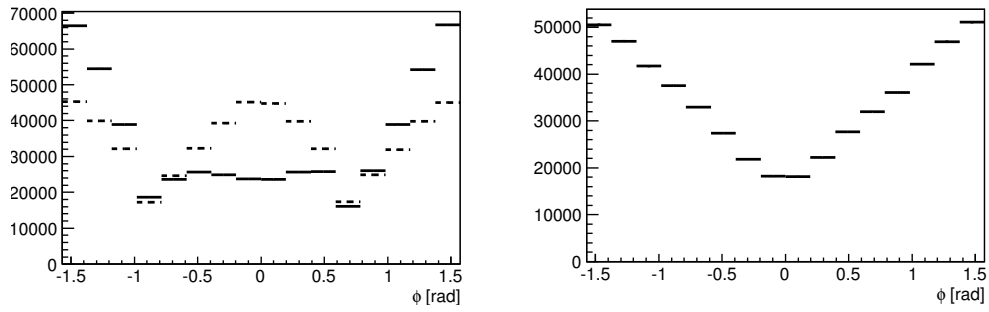
Figure 3.8. The left panel shows distribution of azimuthal scattering angles for a polarized beam (solid lines) and an unpolarized beam (dashed lines). The right panel shows distributions of azimuthal scattering angles for a polarized X-ray beam after correcting for binning effects. All events triggering one or more CZT detectors have been used in the analysis.
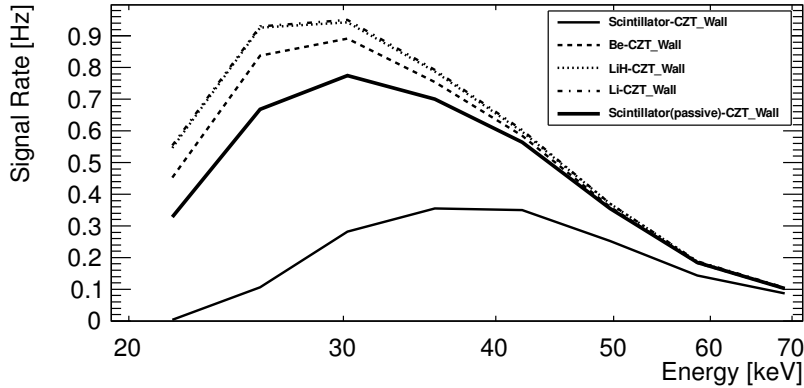
Figure 3.9. The detection rate of Compton events for scattering sticks made of various materials (assuming a balloon flight with X-Calibur and the Nagoya University mirror at an altitude of 130,000 feet). The calculation assumes a source with a Crab-like flux and energy spectrum. The different lines show the results for the different scattering sticks and, for the scintillator stick, for different trigger requirements.

distribution shows a modulation owing to the large pixel size (2.5 mm) and associated aliasing effects. Before computing the MDP with Equs.3.1 and 3.2 I correct for binning effects by dividing the polarized distributions by the unpolarized distributions. The correction attens the ϕ-distributions of the unpolarized beams and leads to a sinusoidal modulation of the ϕ-distributions of the polarized beams (see right panel of Figure 3.8. See [14] for a detailed description of the correction procedure and for a study of the validity of Equ. 3.2 when the correction is used. X-Calibur achieves modulation factors of ~ 0.5 (see Table 3.3 and Figure 3.11).

Table 3.2

Sizes of different scattering sticks and CZT detector assemblies discussed in the text.

	Design 1	Design 2	Design 3	Design 4
Scatterer	Scintillator EJ-200	Be	LiH	Li
Diameter	1.3 cm	1.3 cm	1.3 cm	1.3 cm
Length of Scatterer	14 cm	9 cm	18 cm	32 cm
CZT Unit	$0.2 \times 2 \times 2 cm^3$	$0.2 \times 2 \times 2 cm^3$	$0.2 \times 2 \times 2 cm^3$	$0.2 \times 2 \times 2 cm^3$
Length of CZT assembly	16 cm	12 cm	20 cm	34 cm

3.5.2 Performance with 4 different scattering materials

I compared the performance achieved with a scintillator scattering stick with that achieved with scattering sticks made of alternative materials, i.e. Be, Li and LiH. Table 3.2 lists the physical characteristics and dimensions of the different scattering sticks and the CZT detector assemblies for each case. When a plastic scintillator is used as the scattering material, the stick is read out with a photomultiplier. The other three scattering materials are assumed to be passive. The length of all scattering sticks was chosen to yield a Compton scattering probability of 90% for 80 keV photons. The most important results, including the rates of Compton events for a Crab like source RCrab [Hz], the peak detection efficiency and the energy at which this efficiency is achieved, the modulation factor μ and the Minimum Detectable Polarization MDP, are discussed below and are summarized in Table 3.3.

Note that the background for most competing polarimeter designs is indeed high as they have wide field of views and use very massive detectors [14]. However, the
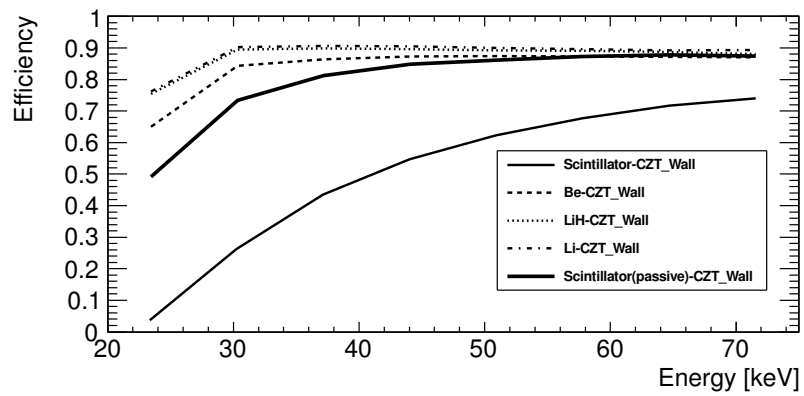
Figure 3.10. The energy dependence of the detection efficiency (number of detected events divided by the number of photons incident on the polarimeter)
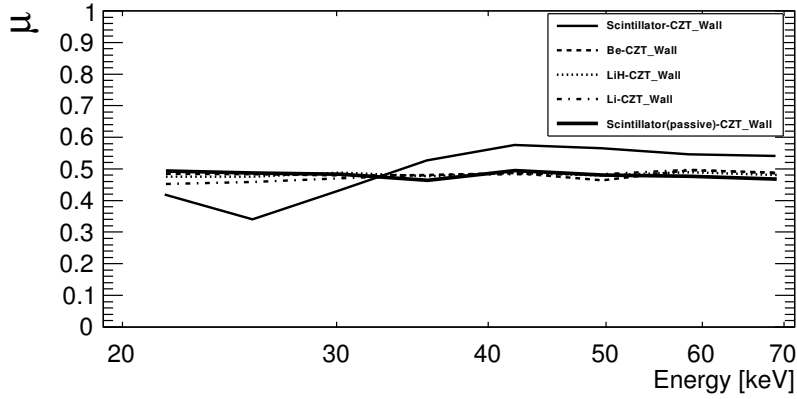
Figure 3.11. Comparison of the modulation factor. The binning was chosen to have 8 statistically independent bins spaced logarithmically between 20 keV and 75 keV. The different lines show the results for different scattering materials. The lines between the data points are only shown to guide the eye.

X-Calibur background is much lower-as I use focusing optics and a thick shield. The residual X-Calibur background is almost negligible for strong sources (like the Crab Nebula). For such sources (i.e. all the sources that X-Calibur will observe during the first balloon flight), it pays off to use all events-even if they do not have a trigger signal in the scintillator. For weak sources and long observations it becomes advantageous to use the scintillator trigger. For example, for a 10^6 s observations of a 25 mCrab source, the MDP is 4.5% when I require the scintillator to be triggered while it is 5.5% for the case without scintillator trigger requirement.

Figure 3.9 and Figure 3.10 shows the detection rates and the detection efficiencies achieved with the different scattering sticks. In Figure 3.9, the thick solid line shows the detection rates without the trigger requirement in the scintillator (i.e. using the

stick as a passive scatterer) while the thin solid line shows the detection rates with a 2 keV threshold in the scintillator. The efficiency is defined here as the fraction of the photons impinging on a detector assembly that trigger the instrument and enter the polarization analysis for an ideal thin beam. The simulations show that the lower-Z materials lead to higher rates and efficiencies, especially at <50 keV energies. The scintillator (solid line) gives the lowest rates and efficiencies while LiH (dash-dotted line) gives the highest. The high efficiencies of the X-Calibur design close to 100% can be explained by the fact that with ideal X-ray mirrors, all source photons hit the scattering stick, a large fraction of the photons Compton scatter in the low-Z material, and most of the scattered photons can escape the stick and are detected in the CZT detectors. The modulation factors are close to 0.5 for all four scattering sticks (Figure 3.9). The LiH scatterer achieves the best MDP (3.02%) followed by Li (3.06%), Be (3.13%), and the Scintillator (4.5% when scintillator triggered at a 2 keV threshold while 3.41% when using it as passive scatterer) (Figure 3.12). The lower-Z materials perform better, but the scintillator can be read by a PMT to give a coincidence signal to identify proper Compton events. As mentioned above, I use the scintillator for the first X-Calibur flight as it allows us to perform detailed tests of the performance and backgrounds of the polarimeter. Note that the <25 keV polarimeter response is relatively more important in space than for a balloon-borne mission (in the latter case, the atmosphere absorbs most of the <25 keV flux). In a space borne mission, a LiH scattering stick performs much better than a scintillator stick and would be our preferred choice.

Table 3.3

Comparison of the performance achieved with the four different scattering materials.

	Scintillator -CZT	Scintillator (passive)-CZT	Be-CZT	LiH-CZT	Li-CZT
$R_{Crab(InFO\mu CS)[Hz]}$	1.58	3.68	4.17	4.46	4.49
Peak efficiency	0.76 (69 keV)	0.87 (65 keV)	0.86 (70 keV)	0.87 (65 keV)	0.88 (70keV)
μ	0.52	0.48	0.48	0.48	0.47
MDP	4.5 %	3.4%	3.1 %	3.1%	3.0%
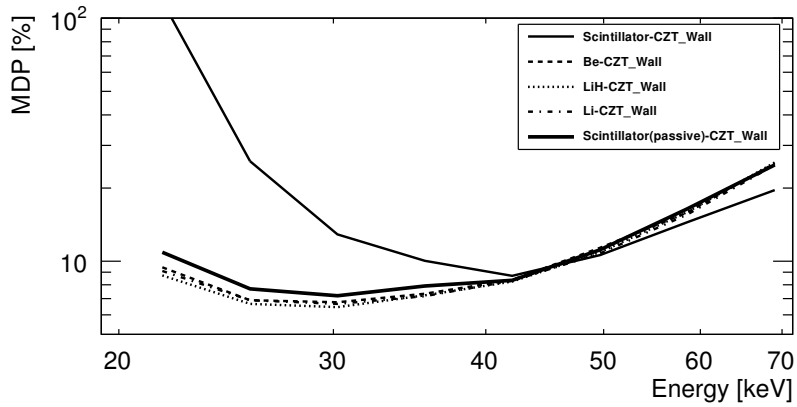
Figure 3.12. Comparison of the MDP for a one-day 5.6 hrs on-source observation of the Crab Nebula with X-Calibur and the Nagoya University mirror. The different lines show the results for different scattering materials.
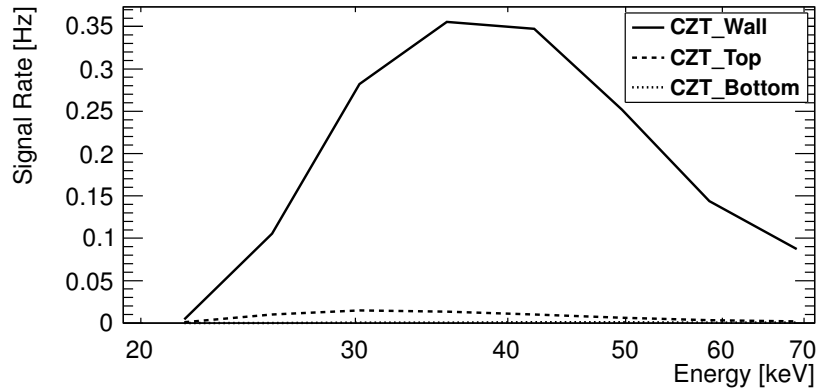
Figure 3.13. Comparison of detection rates in the CZT walls and in the additional CZT detectors at the front-side and rear end of the CZT detector assembly of the reference design Figure 3.3.

3.5.3   Performance with additional CZT detectors

In this section I discuss the performance improvement achieved with additional CZT detectors placed at the two ends of the CZT detector assembly (see the white rectangles in the left panel of Figure 3.3). I use the same assumptions as in the previous sections. Figure 3.13 shows the simulated detection rates: (i) in the standard detector assembly, (ii) in the additional CZT detector at the front-side of the detector assembly, (iii) in the additional CZT detectors at the rear end. The simulation results show that the detection rates in the additional CZT detectors are very low. The reference X-Calibur design thus does not include the additional detectors.

3.5.4 Performance of the 8 CZT detector rings

The CZT detector configuration of X-Calibur is made of 8 rings of four detectors each (32 detector units altogether). In the following, I number the detector rings from 1 at the front end to 8 at the rear end of the assembly (Figure 3.3). The left panel of Figure 3.14 shows the detection rates for all 8 rings. The right panel of the same figure shows the MDPs achieved with the different rings. Owing to the geometry of the scintillator/CZT detector configuration, ring #2 sees most events as it detects forward, backward, and sideward scattered photons. From ring #3 to ring #8, fewer and fewer events are detected, as most of the events are scattered near the front end of the scintillator. Ring #1 sees a substantial number of events, but less than ring #7, because it can only detect backscattered photons.

I simulated the energy spectra detected in each ring of CZT detectors to study how the energy resolution deteriorates owing to the fact that the primary photons deposit some energy in the scintillator, which I cannot measure accurately owing to the scintillator's poor energy resolution. Photons with energies of 20, 60, and 80 keV were generated and the simulations accounted for an inherent RMS energy resolution of the CZT detectors of 2 keV. Figure 3.15 shows energy spectra for 20 and 60 keV photons, and Figure 3.16 shows the energy resolution for each detector ring. The energy resolution is better at lower photon energies owing to the smaller relative fraction of energy lost to the Compton electron. The CZT ring #8 has a better energy
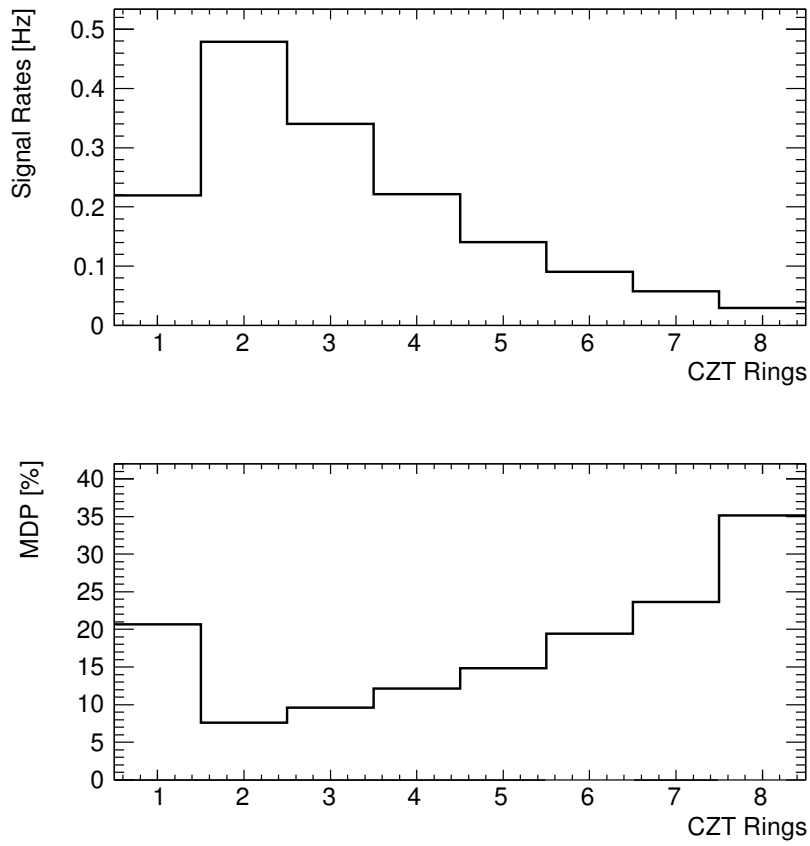
Figure 3.14. Comparison of detection rates (upper panel) and MDPs (lower panel) in different CZT Rings. Ring #1 is at the front side of the detector assembly and ring #8 at the rear end.
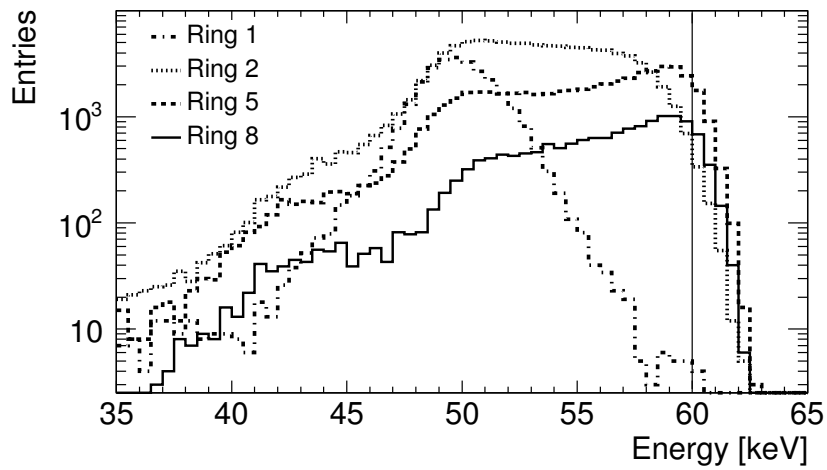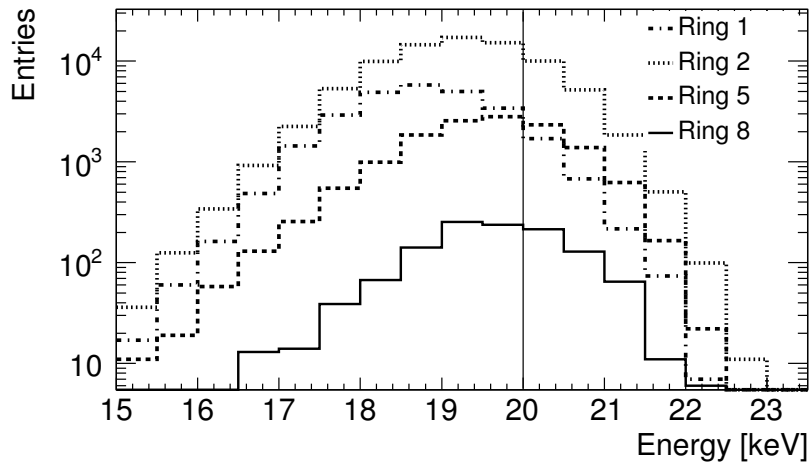
Figure 3.15. The top panel shows the energy depositions measured in CZT rings # 8, # 5, # 2 and # 1 when a 20 keV photon beam Compton scatters in the scintillator. The bottom panel shows the same for a 60 keV photon beam. The simulations include an energy resolution with a RMS of 2 keV.

resolution than the other 7 CZT rings because it only sees backscattered photons with

a narrow range in scattering angles.
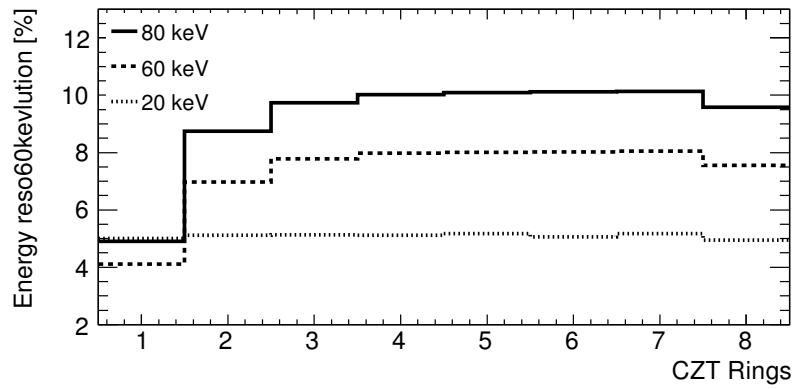
Figure 3.16. Energy resolutions of each CZT ring for 20 keV, 60 keV and 80 keV photons. The energy resolution is the RMS value of the detected energy divided by the mean amplitude.
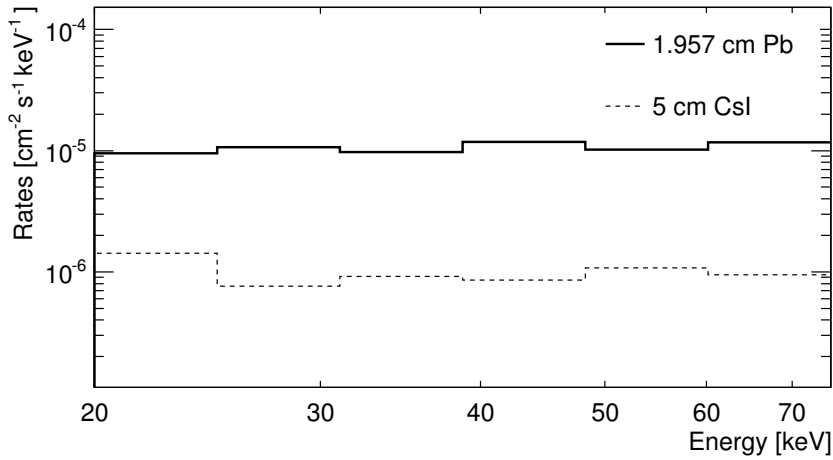
Figure 3.17. Residual background rate for the active/passive shield design.

3.5.5 Optimization of the shield design

I computed the residual background level for different shield designs. I compared the performance achieved with the 5 cm active CsI shield with that of a passive Pb shield with the same mass (wall thickness 1.96 cm). Figure 3.17 shows the background rates in the CZT detectors for the two shields. The active shield used with a 50 keV active veto threshold outperforms the passive shield of the same mass by one order of magnitude in terms of the residual background rate. I simulated active shields with wall thicknesses of 3, 5, and 7 cm. Figure 3.18 shows the residual background energy spectrum for these shield configurations. The residual background rate decreases monotonically with the thickness of the active shield. For our balloon flight, the dominating background comes from the albedo photons (upward secondary γ-rays) from the earth side. Our simulation studies show that a thick active shield suppresses
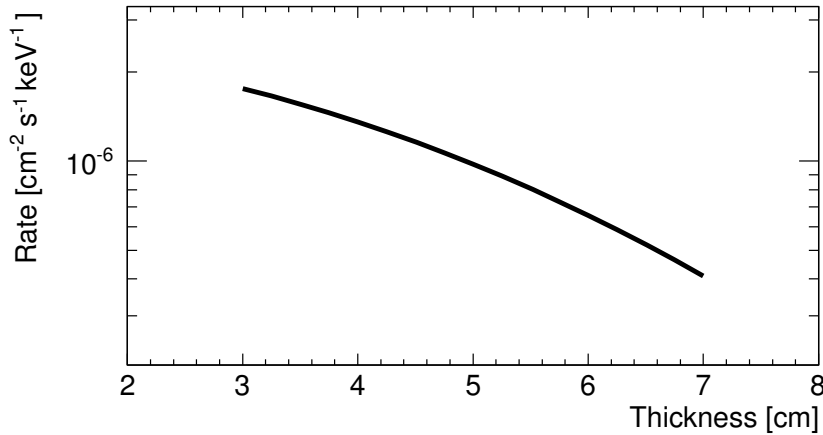
Figure 3.18. Residual background rate of the reference design (active CsI shield, passive Pb front end) as function of the thickness of the active shield.

this background most effectively. The balloon flight results from Slavis et al. [93, 94] back up the results. Balancing the background rejection power with the mass and complexity of the shield, I choose a 5 cm CsI (Na) shields with a 2 cm passive front shield as our reference design (Figure 3.3).

Table 3.4 shows the contributions of different background components to the total background rate for the reference design and a veto energy threshold of 50 keV. As expected, the secondary γ-rays are the main contributor to the residual background rate. Figure 3.19 shows the residual background rate as function of the CsI (Na) energy threshold. The rate increases with the veto threshold of the shield. I choose 50 keV as the veto trigger threshold of the CsI (Na) active shield leading to a residual background rate of 0.007 Hz. The veto rates in the active shields are 57.21 Hz. As-
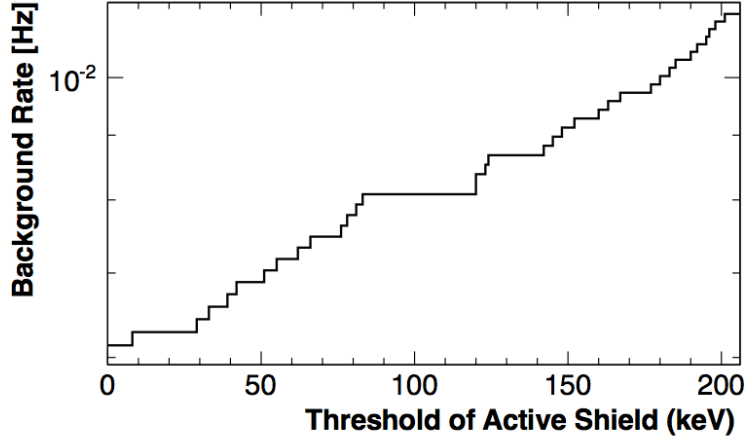
Figure 3.19. The residual background rate as function of the CsI (Na) veto threshold for the same flight altitude. I assume a veto threshold of 50 keV for our sensitivity estimates.

Table 3.4

Contributions of different background components in $cm^{-2}s^{-1}keV^{-1}$ to the total background rate for the reference design and a veto energy threshold of $50\,keV$.

	CXB	Secondary γ-rays	Protons	Electrons
with scintillator trigger	1.3×10^{-8}	9.8×10^{-7}	6.5×10^{-11}	2.1×10^{-9}
no scintillator trigger	6.8×10^{-8}	2.0×10^{-5}	3.9×10^{-10}	2.8×10^{-8}

suming that each background hit vetoes the CZT detectors for 5 μsec, the background

will cause a dead time of 0.03%.
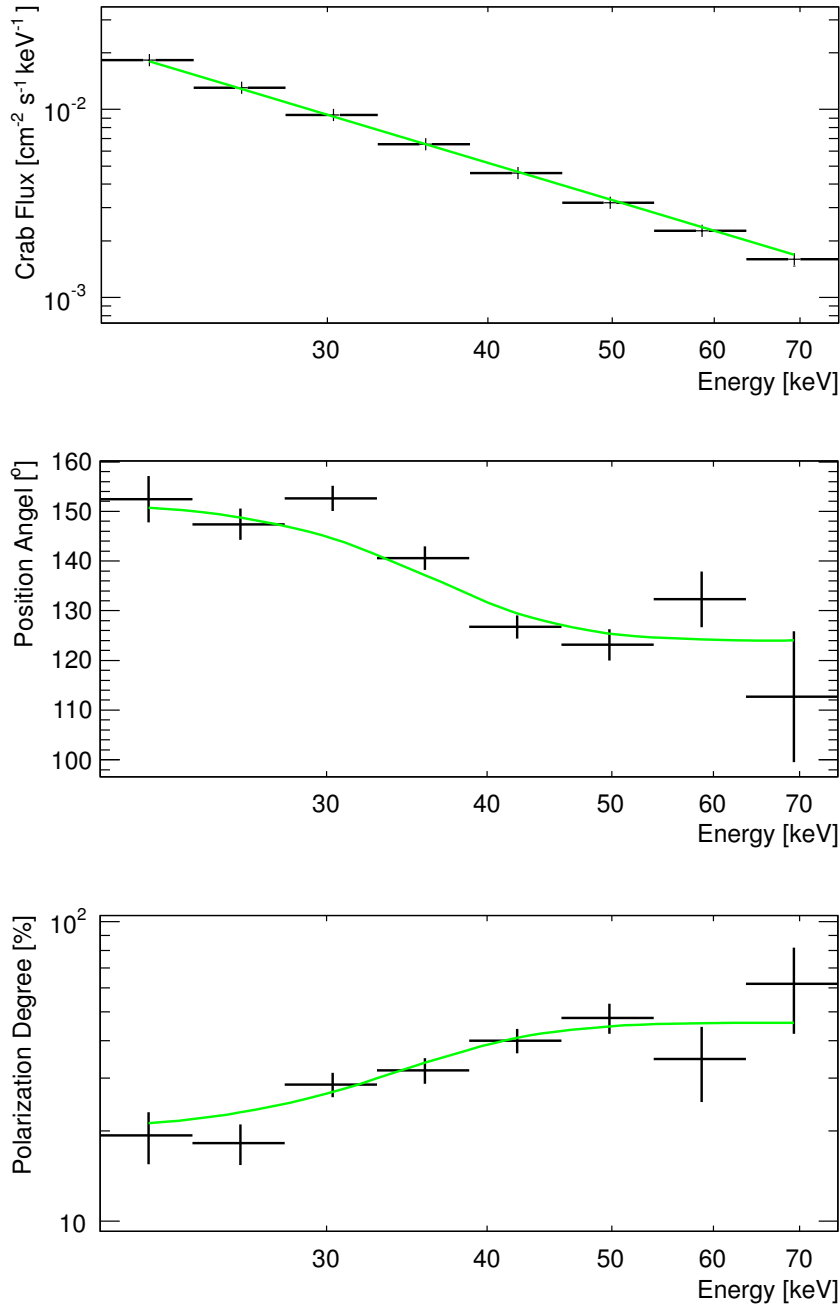
Figure 3.20. Simulated outcome of a 5.6 hrs on-source observation of the Crab Nebula (from top to bottom: Reconstructed flux, reconstructed polarization degree, and reconstructed polarization direction) with X-Calibur and the Nagoya University mirror for a balloon flight altitude of 130,000 feet. The green lines show the assumed model distributions: the Crab spectrum is from [86]; I assume the polarization degree and direction change continuously from the values measured at 5.2 keV with OSO-8 [48] to the values measured at 100 keV with INTEGRAL [61].

3.5.6 Predicted sensitivity of X-Calibur when flown on balloons

On the one-day balloon flight from Fort Sumner, we expect to be able to observe several sources, including the Crab pulsar and nebula, for a few hours. Simulations performed for sources at different zenith angles θ, show that R_{src} scales proportional to $cos^{1.3}\theta$). I use this scaling law when estimating MDPs. Assuming a 5.6 hrs observation of the Crab X-Calibur achieves a Minimum Detectable Polarization degree (MDP, 99% confidence level) of 4.5%. Figure 3.20 shows the outcome of a 5.6 hrs on-source observation of the Crab Nebula (from top to bottom: Reconstructed flux, reconstructed polarization degree, and reconstructed polarization direction) with X-Calibur and the Nagoya University mirror for a balloon flight altitude of 130,000 feet. The graphs show that the observations will give precise measurements of the polarization degree and the polarization direction in several independent energy bins. We plan to follow up on the first balloon flight with proposals for Long Duration Balloon (LDB) flights. An attractive option is a LDB flight with a larger X-ray mirror assembly and then X-Calibur would extend the spectropolarimetric coverage to 60 keV. For a 3-day balloon flight from Alice Springs, X-Calibur/InFOCμS achieves a Minimum Detectable Polarization degree (MDP, 99% confidence level) of 2.6% for a 16.8 hrs observation of a source with a Crab-like flux and energy spectrum. For a 3-week balloon flight from McMurdo, estimating the background to be about 5.5 times higher than that of the balloon flight from Fort Sumner, the MDP would go

down to $\sim1.0\%$ in a 117 hrs on-source observation. Additional mirror modules could reduce the MDP well below the 1.0% limit.

3.6 Summary

In this chapter I described the optimization of the design of the X-Calibur Compton polarimeter by comparing the performance achieved with four different Compton scattering materials (scintillator, Be, LiH, Li), with different CZT detector assemblies, and with several shield configurations. The conclusions from my study can be summarized as follows:

- X-Calibur combines a detection efficiency of order unity with a high modulation factor of $\mu \sim 0.5$. The detection efficiency and the modulation factor have values close to the maximum theoretically possible values given the physics of Compton scatterings.

- The lower-Z scattering sticks (i.e. Be, LiH and Li) perform better than higher-Z scattering sticks (e.g. scintillator), especially at <20 keV energies. As the atmosphere absorbs most of the <20 keV X-rays, we decided to use a scintillator stick for the first balloon flight. The trigger information from the scintillator will allow us to perform additional tests of our simulation model.

- Additional CZT detectors at the front and rear ends give only a marginal improvement of the detection efficiency. On a balloon-borne mission, upward secondary γ-rays dominate the non-vetoed background rate. The simulations

predicted a non-vetoed background rate of $9.8 \times 10^{-7} cm^{-2} s^{-1} keV^{-1}$ (with a >2 keV energy deposition in the scintillator stick and a 20 $\sim$75 keV energy deposition in a CZT detector) and $2.0 \times 10^{-5} cm^{-2} s^{-1} keV^{-1}$ (a 20$\sim$75 keV energy deposition in a CZT detector with no scintillator trigger requirement).

- I derived excellent Minimum Detectable Polarization degrees (MDP, 99% confidence level) of the Crab Nebula: 3.4% for a 1-day balloon flight from Fort Sumner with 5.6 hrs ON-source observation; 2.0% for a 3-day balloon flight from Alice Springs with 16.8 hrs ON-source observation; 0.7% for a 3-week balloon flight from McMurdo with 117.6 hrs ON-source observation.

4. Broad band scattering polarimeter

4.1 Photon electron interaction processes at soft and intermediate X-ray energies

In a scattering process, the cross section is proportional to the square of the quantum mechanical amplitude. Different processes dominate in different energy bands. In the following I focus on the 2-75 keV energy band in which a scattering polarimeter used in the focal plane of a focusing mirror can be operated. In principle scattering polarimetry works to even higher energies as the Compton effect is the dominant interaction process to energies exceeding 2 $m_e c^2 \approx 1$ MeV, when pair production processes start to dominate. The 75 keV limit mostly comes from the cutoff of the mirror reflectivity. At photon energies below 100 keV the following three interaction processes dominate: atomic photoelectric absorption, coherent (Rayleigh scattering off electrons moving in the nuclear Coulomb field) and incoherent (Thomson/Compton) scattering off quasi-free valence electrons. In this section, I discuss how one can extend the energy range of a scattering polarimeter toward lower energies. The X-Calibur polarimeter loses efficiency below ∼20 keV, as at those energies photoelectric effect interactions dominate strongly over scattering interactions. We can maximize

the probability for a scattering interaction by using a lower-Z scatterer. The best practical materials are Li and LiH, as the H an Li are not dense enough.

Figure 4.1 shows the dominant interaction processes in LiH. At energies below $\sim$10 keV, photoelectric effect interactions dominate over coherent and incoherent scattering interactions. A scattering polairmeter thus works best at energies above 10 keV. However, most astrophysical sources exhibit a steeply falling energy spectrum with many more photons at lower energies than at higher energies. As a result, it is attractive to use a scattering polarimeter even in the soft energy regime from a few keV to 10 keV.

Figure 4.1 shows that coherent (Raleigh) scattering dominates over incoherent (Thomson/Compton) scattering up to approximately 6 keV. However, above 6 keV, the latter starts to dominate. Although different scattering processes dominate at different energies, all scattering processes share the property that the photons scatter preferentially perpendicular to the direction of the electric field vector. Thus, for a scattering polarimeter it does not matter if the photons Raleigh or Thomson/Compton scatter. When a photon scatters on a bound electron, it deposits little energy to the recoiled atom. So, in the Raleigh regime, the energy resolution of a scattering polarimeter is particularly good and is only limited by the energy resolution of the detectors. S. Tashenov et al. [95,96] discuss a hard X-ray polarimeter that uses mainly Raleigh scatterings.
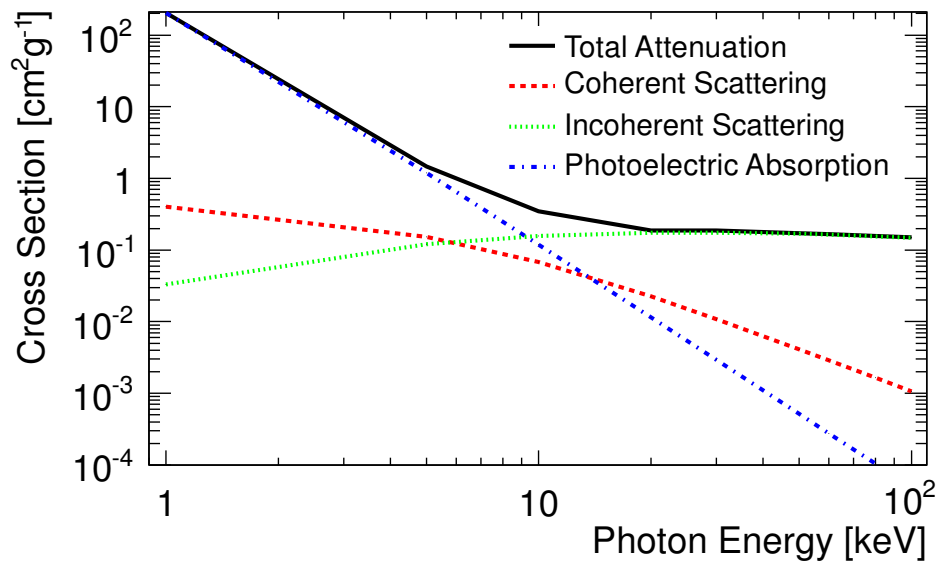
Figure 4.1. Cross sections for interactions in LiH. Compton (incoherent) scattering dominates over the energy range from 10-100 keV as shown. At the energies below 6 keV, Rayleigh scattering dominates over Compton scattering.

Table 4.1

Required length of scattering stick to absorb 90% of the incoming photons.

Absorption (90%)	5 keV	60 keV
Li	3.16 cm	30.73 cm
LiH	2.47 cm	18 cm

4.2 Broadband X-ray polarimeter

In this section, I discuss the design of an X-ray polarimeter with an extended energy bandpass. I focus in particular on a broadband polarimeter with sensitivity to the soft X-ray band below 10 keV. For a balloon borne experiment like X-Calibur, the <10 keV sensitivity is not relevant, as the atmosphere absorbs <20 keV photons even at the 125,000 feet altitudes of stratospheric balloon flights. However, a space-borne scattering polarimeter could be used in the 2-20 keV energy range.

A polarimeter using LiH or Li as the scatterer would have to be longer to achieve a high detection efficiency. I calculate that an 18 cm long LiH slab and a 30.73 cm long Li slab would be required to absorb >90% of the incoming photons for energies from 2 keV to 75 keV (see Table 4.1). A polarimeter could be built to enclose the LiH or Li scatterer with a CZT detector assembly which is slightly larger than the LiH or Li slabs (Figure 4.2). The scattering slabs would have to be encased in a thin (0.5 mm) Be layer to avoid the reaction of the LiH or the Li with ambient humidity and oxygen.
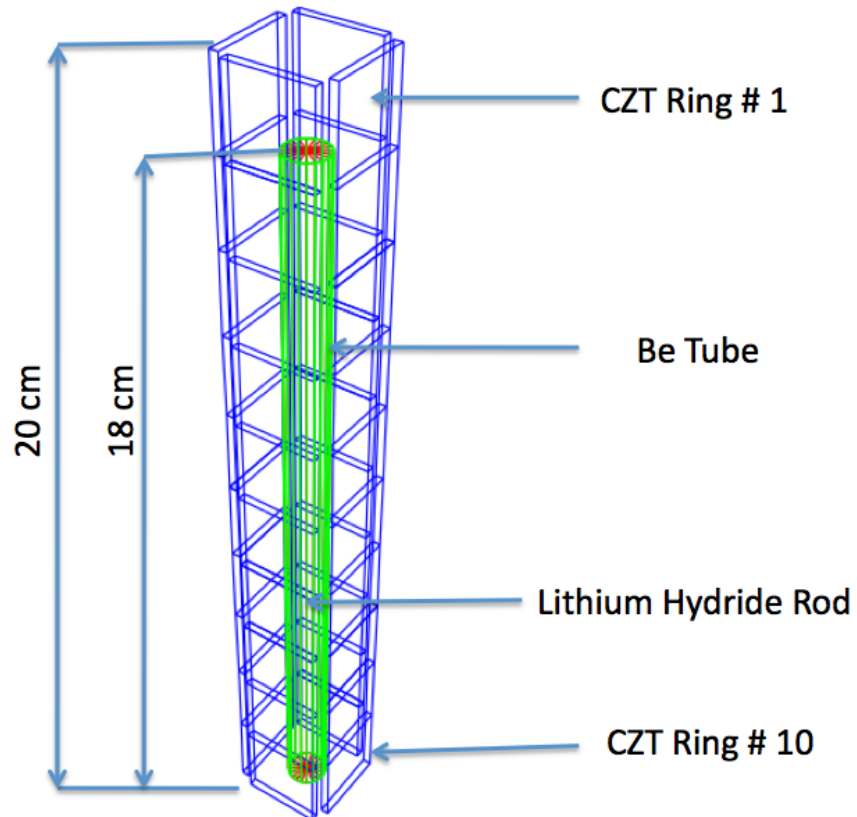
Figure 4.2. Conceptual design of the broadband X-ray polarimeter consisting of a scattering LiH slab (red) with Be housing (green) surrounded by absorbing CZT detectors (blue). The scattering slab is aligned with the optical axis of an X-ray mirror (not shown here). A large fraction of the scattered photons are subsequently photo-absorbed in the high-Z CZT detectors.

4.3 Performance estimate

I ran Monte Carlo simulations to estimate the sensitivity that such a broadband polarimeter could achieve when used with a single X-ray mirror [97] similar to the one used on the NuSTAR X-ray telescope. The Monte Carlo simulations use the Geant4 simulation package [84] and the Livermore Low-Energy Electromagnetic Models physics list. I used the published NuSTAR background spectrum to add background noise to our calculations [97]. Photons with energies between 14 keV and 75 keV were generated according to the Crab spectrum as measured with the Swift Burst Alert Telescope (BAT) telescope [86], as shown in Equ. 3.3. Photons with energies between 2 and 14 keV were generated according to the Crab spectrum from the XMM-Newton observations of the Crab [98], as shown in Equ. 4.1. The spectrum is almost the same as Equ. 3.3.

$$\frac{dN}{dE} = 9.59 \left(\frac{E}{1keV} \right)^{-2.108} ph\, cm^{-2}s^{-1}keV^{-1} \tag{4.1}$$

The simulations assume a 18 cm long LiH scatterer with 1 cm diameter, surrounded by a 20 cm long CZT detector assembly (40 CZT detectors, each made of $2 \times 20 \times 20$ mm^3 CZT crystals). Every CZT ring covers the whole 360° azimuthal scattering range. A 18 cm long LiH stick turns out to be the best choice for the scatterer.
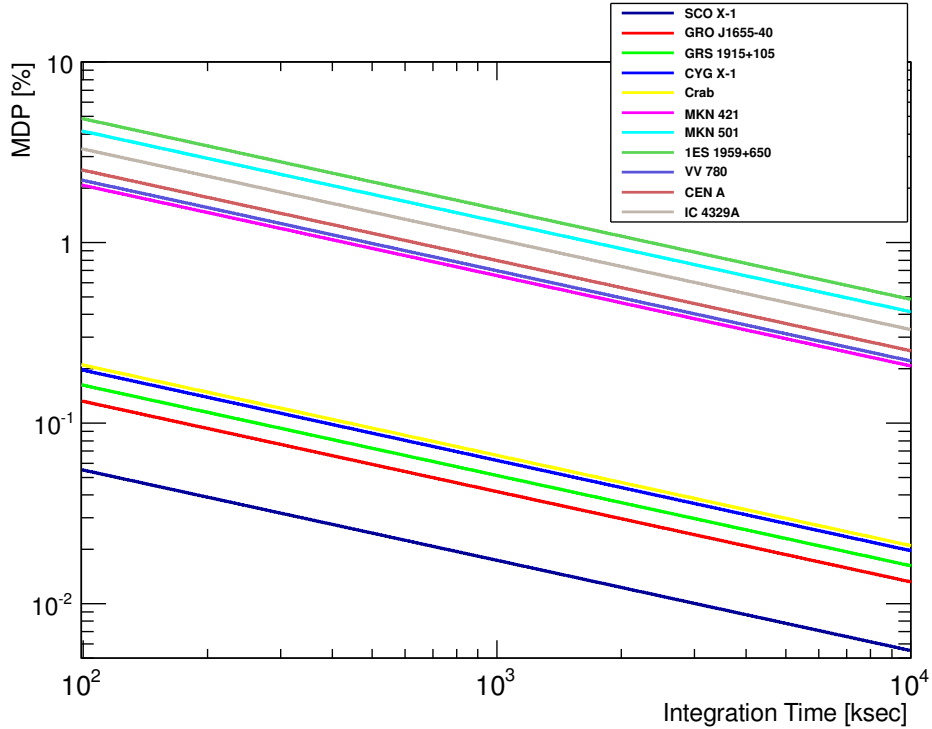
Figure 4.3. MDPs of 11 bright X-ray sources (black holes binaries, blazars and AGNs) in the function of time. The analysis is based on the 2-12 keV data, assuming a NuSTAR-type mirror. With an observation time above 100 ksec, the MDPs of all these 11 sources are well below 5.0%.

4.4 Performance sensitivity based on Monte Carlo simulations

4.4.1 Detection sensitivity of target sources

I estimated the sensitivity of the broadband X-Calibur like polarimeter based on the Monte Carlo studies making use of the energy dependent effective area of the NuSTAR-type mirror assembly averaged over all detector rings and estimating the background level based on the simulations results carried through for NuSTAR [97]. As shown in Equ. 3.2, the MDP is inversely proportional to the square root of time.
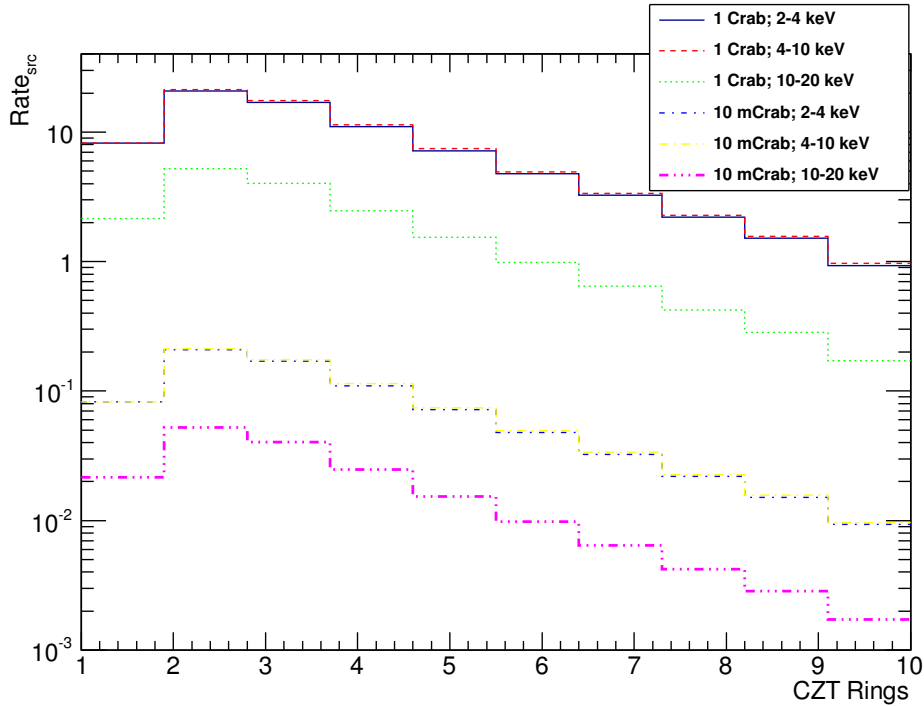
Figure 4.4. Comparison of detection rates achieved in different CZT Rings in different energy ranges and different sources. Ring #2 sees most photons.

I calculated the sensitivities of 11 typical sources (black holes binaries, blazars and AGNs) as the function of time (see Figure 4.3). I assumed the time averaged 2-12 keV fluxes measured with the RXTE All Sky Monitor (ASM). With an observation time above 100 ksec, the MDPs of all these 11 sources are well below 5.0%.

4.4.2 Performance of the 10 CZT detector rings

In the following, I number the detector rings from 1 at the front end to 10 at the rear end of the assembly (Figure 4.2). Figure 4.4 shows the detection rates for all 10
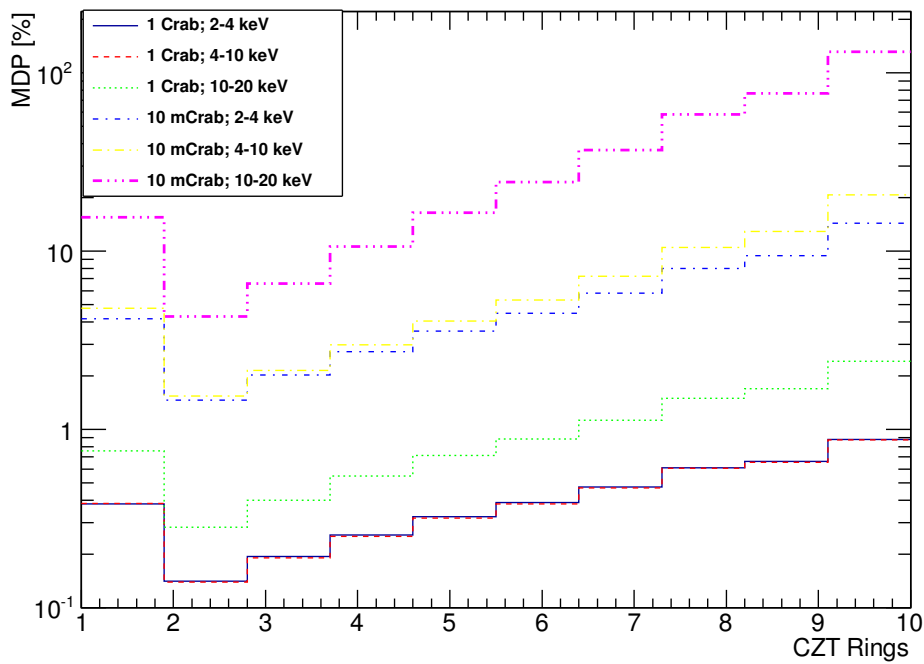
Figure 4.5. Comparison of detection MDPs achieved in different CZT Rings in different energy range and sources. Ring #2 performs best in all cases.
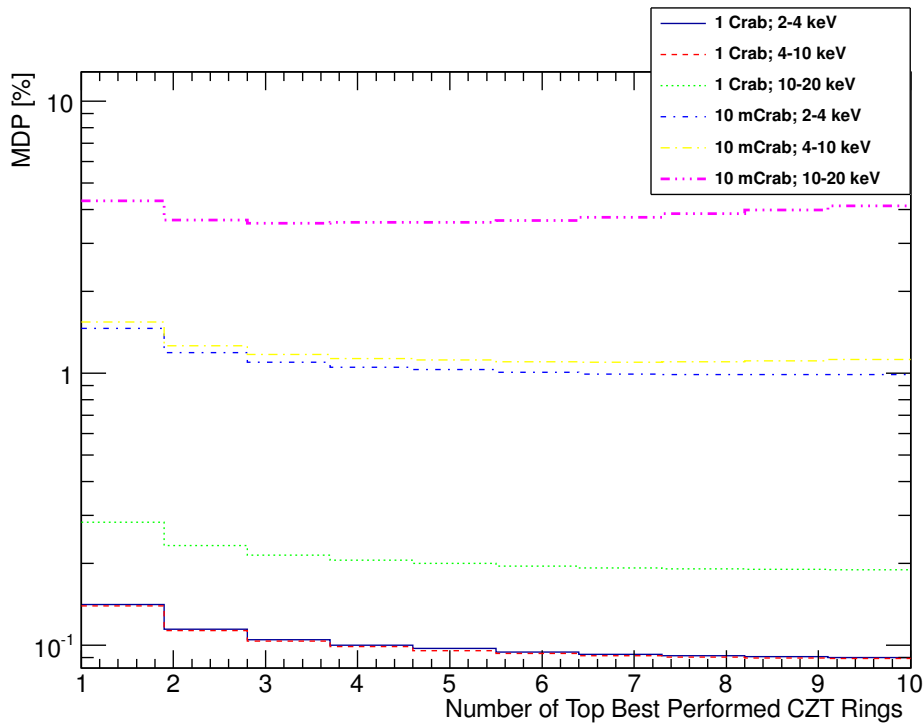
Figure 4.6. MDPs with the best performing rings in different energy ranges and different sources. For bright source like Crab, the lowest MDP is achieved when performed with all the 10 rings. For a week source like 10 mCrab, the best MDP is achieved with the combination of about 5 rings: ring #2, #3, #4, #5 and #1.

rings in different energy ranges for different sources. Owing to the geometry of the LiH/CZT detector configuration, ring #2 sees most events in all cases as it detects forward, backward, and sideward scattered photons. From ring #3 to ring #10, fewer and fewer events are detected, as most of the events are scattered near the front end of the scintillator. Ring #1 sees a substantial number of events, but less than ring #5, because it can only detect backscattered photons. Figure 4.5 shows the MDPs achieved with the different rings in different energy ranges for different sources. Ring #2 achieves the lowest MDP for all cases. For 10 mCrab source, ring #2 achieves the lowest MDP, followed by ring #3, #4, #5, #1, #6, #7, #8, #9 and #10. Figure 4.6 shows the MDPs with the best performing rings of different energy ranges and different sources. For bright source like Crab, the lowest MDP is achieved with all the 10 rings. For a weak source like 10 mCrab, the best MDP is achieved with the combination of 5 rings: ring #2, #3, #4, #5, and #1, as shown in Figure 4.6. With more rings, the background contribution becomes important which deteriorates the MDP. Taking all factors into account, we may use the top 5 best performing rings for our final design.

4.5   Summary

In this chapter I described avenues for extending the energy coverage of the X-Calibur polarimeter towards lower energies. Rayleigh scattering is the dominant scattering process at 2-6 keV while Compton scattering dominates at 6-75 keV energy range. I performed detailed Monte Carlo simulations to study the performance of such

an experiment. LiH is used as the scatterer for the higher efficiency and a shorter required length. The broadband polarimeter is made of 10 rings of CZT detectors (40 detector units altogether) and 18 cm long LiH scattering stick with a diameter of 1 cm. I analyzed the performance of the 10 CZT rings in different energy ranges and sources and Ring #2 outperforms in all cases. For bright source like Crab, the lowest MDP is achieved with all the 10 rings. For a weak source like 10 mCrab, the best MDP is achieved with the combination of the top 5 best performing rings.

5. Scientific potential of blazar observations with a high-sensitivity polarimeter

5.1 Blazar science investigations

Blazars are excellent source targets for X-ray polarimetry experiments as the emission is non-thermal, and the emission processes (synchrotron emission and inverse Compton emission) can lead to high polarization fractions.

The blazars are classified based on their Spectral Energy Distributions (SEDs). HSP, ISP and LSP are used to denote BL Lac subclasses: high synchrotron peaked ($\nu_{peak}^{S} > 10^{15} Hz$) blazars, intermediate synchrotron peaked ($10^{14} Hz < \nu_{peak}^{S} < 10^{15} Hz$) blazars, and low synchrotron peaked ($\nu_{peak}^{S} < 10^{14} Hz$) blazars [105]. FSRQ is used to denote Flat Spectrum Radio Quasars [105].

X-ray polarimetry measurements can be used to study the synchrotron X-ray emission from AGN jets [105]. Polarization swings of the optical synchrotron emission of HSP blazars were reported and studied by Marscher et al. [103] and Abdo et al. [104]. The polarization swings were associated with γ-ray flares. The authors argue that the polarization swings are evidence for a helical magnetic field threading the jet. The helical field is thought to accelerate the jet medium via magnetic stresses and play a key role in collimating the jet. The X-rays (and γ-rays) are hypothesized

71

to come from a stationary (particle accelerating) shock through which the helical magnetic field moves. The synchrotron emission reflects the changing orientation of the magnetic field in the particle acceleration region. As the higher energy X-ray emitting electrons cool faster than lower energy optically emitting electrons, X-rays probe smaller and more uniform emission regions [105]. We thus expect that we see cleaner signatures in X-rays, i.e. higher polarization degrees and more frequent polarization swings. Therefore, X-ray polarimetry measurements of blazars can be used to verify the helical magnetic field structure and to understand the formation, acceleration, and collimation of jets [105].

Inverse Compton emission is an essential radiation mechanism to blazars. For Compton Emission, if the photons from synchrotron emission act as the seed photons in inverse Compton scattering process, it is called Synchrotron Self-Compton Emission (SSC), while it is called External Compton Emission (EC) if the seed photons are from external radiation fields outside of the jet. The polarization properties of the X-rays emission from SSC origin are similar to those of optical synchrotron emission [36, 105–107], while the X-ray polarization fraction is lower than that of optical emission if the X-rays are emitted from EC origin. Therefore, the X-ray polarimetry measurement of blazars is potential to distinguish a SSC from an EC origin of the inverse Compton emission [14, 105, 107].

In hadronic models of the X-ray to γ-ray HSP emission, the X-rays can originate as synchrotron emission from ultra high energy cosmic rays [38, 108, 109]. This model can explain very high polarization degrees ($\sim$70%) if the jet magnetic fields are

uniform and oriented perpendicular to the line of sight (including relativistic aberration effects). Very high polarization degrees would thus favor hadronic over leptonic models.

5.2   Source samples

In this chapter I discuss whether a first-generation X-ray polarimetry mission like a space borne version of X-Calibur or the GEMS and XIPE missions will have sufficiently good sensitivity to address the science questions introduced. These three missions achieve very similar 2-12 keV sensitivities. For this chapter, I assume that they achieve a MDP of 0.7% for a 1.2×10^3 ksec observation of a 10 mCrab source, and that the MDP scales inversely proportional to the integration time. We used two data samples to address this question: (i) the 2 keV-12 keV light curves from the All Sky Monitor (ASM) of the Rossi X-ray Timing Explorer (RXTE) mission [110], and (ii) the 15 keV-50 keV light curves from the Burst Alert Telescope (BAT) [111] of the Swift X-ray observatory [112,113].

The RXTE ASM data set was acquired between January 1996 and January 2012. The analyzed RXTE data was kindly provided to us by Dr. Remillard. The BAT observations were taken between February 2005 and March 2013. The analyzed BAT data were kindly provided to us by Dr. H. Krimm and a description of the data analysis methods can be found in [113].

The ASM catalog contains 69 blazars. In Figure 5.1, I present the Minimum Detectable Polarization (MDP, 99% confidence level) that a mission like X-Calibur,
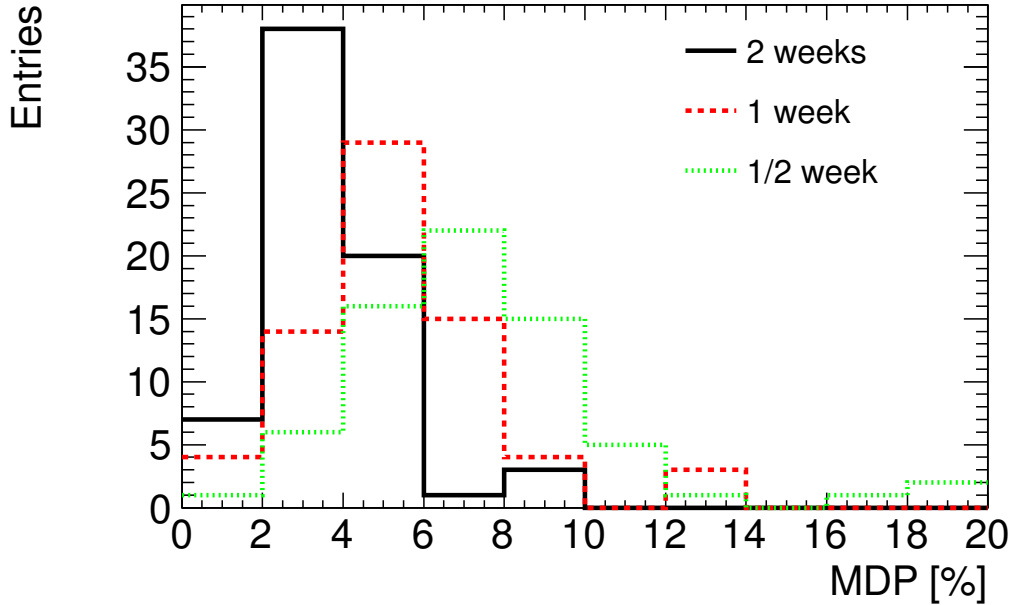
Figure 5.1. Expected MDPs distribution of the 69 blazars for a first-generation polarimeter like X-Calibur, GEMS, or XIPE.

GEMS, or XIPE could achieve for these 69 sources, assuming (i) that the sources emitted at a level equal to their time averaged 2-12 keV RXTE ASM fluxes, and (ii) on-source integration times of between 1/2 week and 2 weeks. Assuming an integration time of two weeks per source, the MDPs lie between 0.6% for Mrk 421, the strongest source in the sample, and 4.5% for 3C 371, the weakest source in the sample. Assuming an integration time of 1/2 week per source, the corresponding MDPs are 1.2% and 8.8%, respectively.

Figure 5.2 shows the two-week MDPs for the different types of blazars, FSRQs, LSPs, ISPs, and HSPs. Here BL Lac refers to the BL Lac type sources for which it
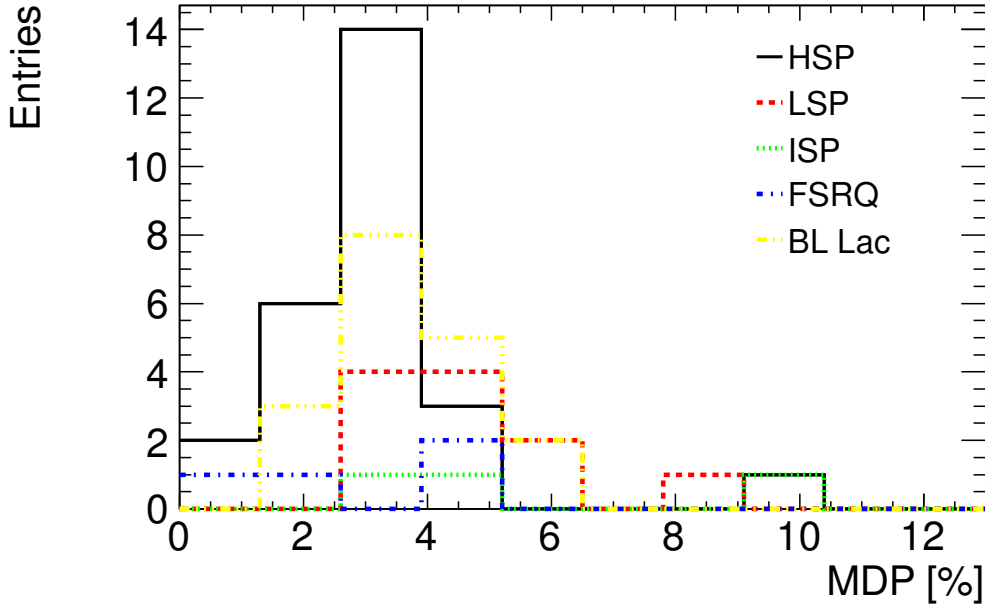
Figure 5.2. MDPs for the different types of blazars, FSRQs, LSPs, ISPs, and HSPs. Here BL Lac refers to the BL Lac type sources for which it is not certain whether they are LSPs, ISPs, or HSPs.

is not certain whether they are LSPs, ISPs, or HSPs. As mentioned above, Mrk 421 is the brightest HSP and the two-week MDP is 0.6%. The brightest FSRQ/LSP is PKS 1510-089 with a two-week MDP of 2.0% and the brightest ISP is 3C66A with a two-week MDP of 3.2%. Figure 5.3 shows the correlation of the MDP and the redshift of the source (for all the sources with archival redshifts). Overall, it is clear that the polarization studies would be limited to nearby low-redshift blazars.

A polarimeter with a similar soft (<10 keV) and hard (>10 keV) sensitivity for a Crab-like source (like X-Calibur) will thus detect more blazars in the soft band than in the hard band. An X-Calibur-like mission could detect the 15-50 keV polarization
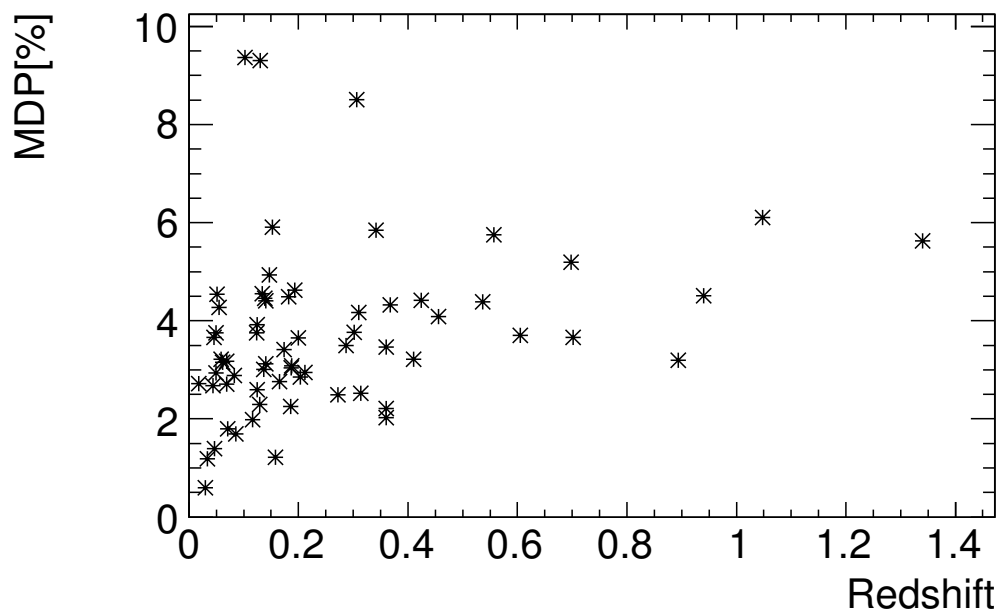
Figure 5.3. Correlation of the MDP and the redshift of the source (for all the sources with archival redshifts).

of a 100 mCrab source with a MDP of 1.5%. With a two-week observation of the brightest HSP Mrk 421, a MDP of 4.7% could be achieved in the energy band 15-50 keV.

5.3 Observation strategy

I compiled a straw-man observation program, assuming that a first generation polarimeter like X-Calibur, GEMS, or XIPE could allocate up to about 3 months of observation time for the study of blazars. The best candidate sources are X-ray bright and exhibit a high polarization fraction at longer wavelengths. However, the flux of a blazar changes on time scales from minutes to decades due to the flares with a "red noise" power spectrum [105]. Therefore, the observation program should be updated at the beginning of the mission and/or during the mission making use of the flux information from ground and space-borne experiments [105].

Probing the role and structure of magnetic fields in AGN Jets requires observations of bright HSPs with a synchrotron component reaching all the way to the X-ray energy band [105]. Table 5.1 lists the brightest targets. The information of the redshift and balzar type of each blazar in this thesis are from [118–122]. With the exception of 1ES 0033+595 and 1ES 1101-232 for which I found no publication about the optical polarization information, the sources exhibit readily detectable polarization degrees of O(5%). Ideally, a first-generation polarimetry experiment should observe a few targets very intensively to study the time variability of the energy spectra and the polarization properties. Such observations could test the hypothesis of a helical

Table 5.1

List of target sources to investigate the structure and role of magnetic fields in AGN jets [105]. Column 4 gives the assumed 2-12 keV energy flux levels in units of mCrab.

Object	Class	z	F_{mCrab} (2-12keV)	Opt. pol [%]
MKN421	HSP	0.03002	13.9	0-13 [114, 115]
MKN501	HSP	0.03366	5.1	2-4 [115]
1ES 1959+650	HSP	0.04700	4.1	5.7 [116]
1ES 0033+595	HSP	0.08600	3.2	
PKS 2005-489	HSP	0.07100	3.0	3.0-11.12 [117]
PKS 2155-304	HSP	0.11600	2.6	3.0-11.86 [117]
PKS 1553+113	HSP	0.36000	2.3	3-7 [115]
1ES 1101-232	HSP	0.18600	2.3	

Table 5.2

List of target sources to investigate the identification of the X-ray to γ-ray emission mechanism in FSRQs and LSPs [105]. Column 4 gives the assumed 2-12 keV energy flux levels in units of mCrab.

Object	Class	z	F_{mCrab} (2-12keV)	Opt. pol [%]
3C 273	FSRQ	0.15834	4.90168	1 [115]
PKS 1510-08	FSRQ	0.36000	2.57003	2-30 [123]
BL LAC	LSP	0.06860	1.51308	2-23 [115]
PKS 0537-441	LSP	0.89400	1.50374	18.8 [124]
BL 0829+046	LSP	0.17368	1.39212	20.5 [124]
3C 279	FSRQ	0.53620	1.05525	2-43 [103, 125]
3C 371	LSP	0.05100	1.01426	11.3 [126]

magnetic field in the blazar zone. The consistent detection of polarization swings in a few sources would suffice to show that helical magnetic field plays the key role in launching and accelerating AGN jets. HSP observation could furthermore be used to study the correlation of the X-ray spectral index and the polarization fraction which constrains the magnetic field configuration in blazar jets.

To investigate the identification of the X-ray to γ-Ray emission mechanism in LSPs [105], it requires the observation of bright FSRQs/LSPs. Table 5.2 lists the prime candidates. Some of the sources exhibit very high degrees of optical polarization reaching several 10%. The observation of sources like 3C 273 and PKS 1510-08 could be used to distinguish between the hadronic origin (polarization fractions exceeding 50%), SSC origin (polarization fractions between 10% and 50%) and EC origin (polarization fractions below 10%). The detection of a single source with a > 50% polarization fraction would argue for the hadronic model. However, observations
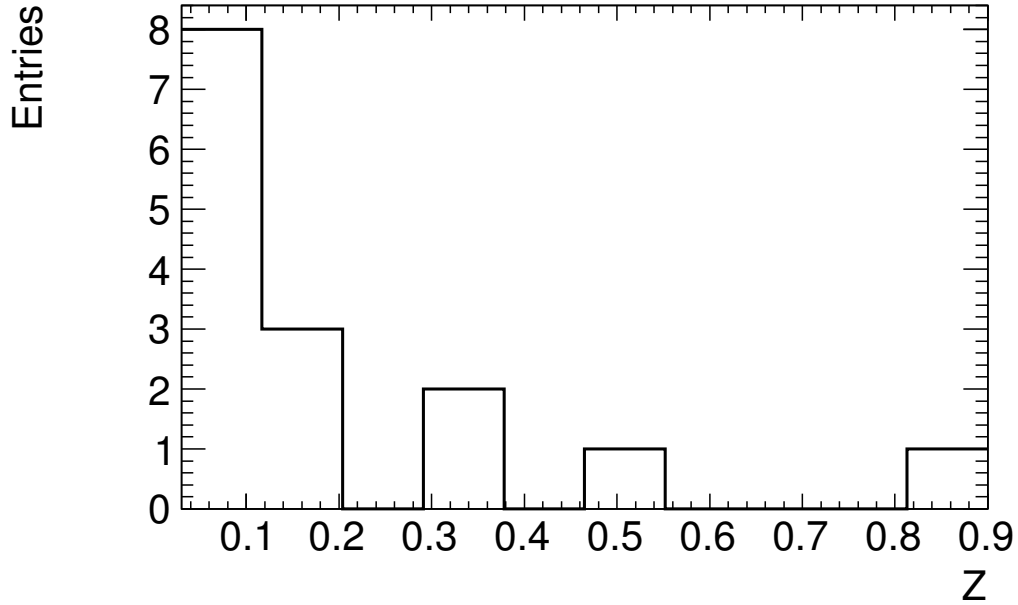
Figure 5.4. Redshift distribution of the selected fifteen target sources.

of many more sources are needed to establish the other two hypotheses as all three hypotheses can predict the detection of low polarization fractions; low polarization degrees are possible in all three models for certain geometries (i.e. when the observer looks right down the jet magnetic field lines).

A straw-man observation program is shown in Table 5.3. The blazars of this sample are moderately distant and have redshifts between 0.03002 and 0.894 (see Figure 5.4).

The HSP Mrk 421 is a prime target with a suggested observation time of two weeks. Tosti et al. reported that the polarization degrees of Mrk421 is between 3% and 16% in the optical range [114]. The polarization fraction is expected to be higher

Table 5.3
Proposed observation program. The total observation time is 14.5 weeks.
Column 5 gives the time averaged 2-12 keV energy flux levels, F1 [mCrab].
Column 7 gives the assumed 2-12 keV energy flux levels, F2 [mCrab], of
the target of opportunity (ToO) program.

Object	Class	z	Time [week]	F1	MDP [%]	F2	MDP [%]
Mkn421	HSP	0.03002	2	13.9497	0.6	56.1151	0.3
Mkn501	HSP	0.03366	1/2	5.05943	2.4	11.2529	1.4
1ES 1959+650	HSP	0.04700	1/2	4.09526	2.8	4.20502	2.7
1ES 0033+595	HSP	0.08600	1/2	3.19162	3.4	5.82951	2.1
PKS 2005-489		0.07100	1/2	2.97384	3.6	9.25563	1.5
PKS 2155-304	HSP	0.11600	1/2	2.63126	4.0	6.27717	2.0
PKS 1553+113		0.36000	1/2	2.31111	4.4	6.27286	2.0
1ES 1101-232	HSP	0.18600	1/2	2.25156	4.5	4.05012	2.8
3C 273	FSRQ	0.15834	1	4.90168	1.7	7.72664	1.2
PKS 1510-08	FSRQ	0.36000	1	2.57003	2.9	3.9211	2.0
BL LAC	LSP	0.06860	1	1.51308	4.5	4.96279	1.7
PKS 0537-441	LSP	0.89400	1	1.50374	4.5	5.55727	1.6
BL 0829+046	LSP	0.17368	1	1.39212	4.8	6.31172	1.4
3C 279	FSRQ	0.53620	2	1.05525	4.4	2.36234	2.2
3C 371	LSP	0.05100	2	1.01426	4.5	2.63513	2.0

at higher energies [114]. With two-week observation of Mrk 421 the MDP can reach 0.6%. From the other fourteen source candidates in Table 5.3, six of them are HSPs, four of them are LSPs and three of them are FSRQs. These sources are the brightest HSPs, LSPs and FSRQs from 2 keV to 10 keV of the RXTE ASM. We envision two observation programs. First, we plan to observe all the candidate sources listed in Table 5.3 without any trigger requirement. We are also considering an alert-driven Target of Opportunity (ToO) program. I estimated the MDPs each source can reach for these two programs. I adapted the exposure time to achieve a <5% MDP for all target sources.

5.4 Summary

I described the scientific potential of blazars observations with a first generation X-ray polarimeter mission like X-Calibur, GEMS and XIPE. I discussed a proposed observation program including observations strategy, sources of interest, recommended accompanying multiwavelength observations, and the observations results. Fifteen sources were selected as target candidates for the science investigations based on the analysis of the daily flux values of all monitored sources by the RXTE All-Sky Monitor (2-12 keV) and Swift BAT 70-month hard X-ray survey (15-50 keV). They are six brightest HSPs, four LSPs and three FSRQs.

I compiled a straw-man observation program, assuming that a first generation polarimeter like X-Calibur, GEMS, or XIPE could allocate up to about three months of observation time for the study of blazars. With two-week observation of Mrk 421

the MDP can reach 0.6% while it reaches 4.5% for 3C 371, the weakest source in the sample. I adapted the exposure time to achieve a <5.0% MDP for all the fifteen target sources.

6. Summary

My thesis focuses on the optimization of the balloon borne X-Calibur scattering polarimeter, to be used in the focal plane of the balloon borne InFOCμS grazing incidence X-ray telescope. The balloon borne version of X-Calibur combines a low-Z scatterer with a CZT detector assembly to measure the polarization of 20-75 keV X-rays, making use of the fact that polarized photons scatter preferentially perpendicular to the electric field orientation.

X-Calibur achieves a high detection efficiency with a high modulation factor of $\mu \sim 0.5$. The lower-Z scattering sticks (e.g. Be, LiH and Li) perform better than higher-Z scattering sticks (e.g. scintillator), especially at <20 keV energies. As the atmosphere absorbs most of the <20 keV X-rays, we decided to use a scintillator stick for the first balloon flight. The trigger information from the scintillator will allow us to perform additional tests of our simulation model. Additional CZT detectors at the front and rear ends give only a marginal improvement of the detection efficiency. On a balloon borne mission, upward secondary gamma rays dominate the non-vetoed background rate. The simulations predict a non-vetoed background rate of $9.8 \times 10^{-7} cm^{-2} s^{-1} keV^{-1}$ (with a >2 keV energy deposition in the scintillator stick and a 20-75 keV energy deposition in a CZT detector) and $2.0 \times 10^{-5} cm^{-2} s^{-1} keV^{-1}$ (a 20-75 keV energy deposition in a CZT detector with no scintillator trigger requirement).

I derived excellent Minimum Detectable Polarization degrees (MDP, 99% confidence level) of the Crab Nebula: 3.4% for a 1-day balloon flight from Fort Sumner with 5.6 hrs ON-source observation; 2% for a 3-day balloon flight from Alice Springs with 16.8 hrs ON-source observation; 0.7% for a 3-week balloon flight from McMurdo with 117.6 hrs ON-source observation.

I studied the possibility of extending the sensitivity of a scattering polarimeter into the soft X-ray regime by using a lower-Z LiH scatterer. Rayleigh scattering is the dominant scattering process at 2-6 keV, while Compton scattering dominates at 6-75 keV energy range. I performed detailed Monte Carlo studies to study the sensitivity of such an experiment.

The broadband polarimeter is made of 10 rings of four CZT detectors each (32 detector units altogether) and 18 cm long LiH scattering stick with a diameter of 1 cm. The LiH is used as scatterer to replace the scintillator for higher efficiency and shorter required length. I analyzed the performance of the 10 CZT rings of different energy range and sources and Ring #2 outperforms in all cases. For bright sources like the Crab, the lowest MDP is achieved with all the 10 rings. For a weak source around 10 mCrab, the best MDP is achieved with the combination of the top 5 best performing rings.

Lastly, I described the scientific potential of blazar observations with a first generation X-ray polarimeter mission like X-Calibur, GEMS and XIPE. I present a proposed observation program including observations strategy, sources of interest, recommended accompanying multiwavelength observations, and the observations results.

Fifteen sources were selected as target candidates for the science investigations based on the analysis of the daily flux values of all monitored sources by the RXTE All-Sky Monitor (2-12 keV) and Swift BAT 70-month hard X-ray survey (15-50 keV). They are six brightest HSPs, four LSPs and three FSRQs.

I compiled a straw-man observation program, assuming that a first generation polarimeter like X-Calibur, GEMS, or XIPE could allocate up to about three months of observation time for the study of blazars. With two-week observation of Mrk 421 the MDP can reach 0.6% while it reaches 4.5% for 3C 371, the weakest source in the sample. I adapted the exposure time to achieve a <5.0% MDP for all the fifteen target sources.

REFERENCES

[1] Seward, F. D. & Charles, P. A., 2010, "Exploring the X-ray Universe," Cambridge University Press; 2nd edition, New York.

[2] Giacconi,R., Branduardi, G., Briel, U., et al., 1979, ApJ., 230, 540

[3] Trumper, J. 1983, Adv. Space. Res., 2, No. 4, 241

[4] Weisskopf, M. C. et al., 2002, Publ. Astron. Soc. Pacif. 114, 1

[5] Struder, L., Briel, U., Dennerl, K., et al., 2001, A&A, 265, L18

[6] Jahoda, K., Swank, J., Giles, A.B., et al., 1996, Proc. SPIE, 2808, 59

[7] Mitsuda, K. et al., 2007, PASJ, 59, S9

[8] P. Meszaros, R. Novick, A. Szentgyorgyi, G. A. Chanan, and M. C. Weisskopf, "Astrophysical implications and observational prospects of X-ray polarimetry," ApJ 324, pp. 10561067, Jan. 1988.

[9] Lei, F., Dean, A. J. & Hills, G. L., 1997, SSRv 82, 309.

[10] Rybicki, G. B. and Lightman, A. P., 2004, "Radiative processes in astrophysics, New York," Wiley-Interscience, 169 p.

[11] Ginzburg, V. L.; Syrovatskii, S. I., 1965, "Cosmic Magnetobremsstrahlung (synchrotron Radiation)," Annual Review of Astronomy and Astrophysics, vol. 3, p.297

[12] Elder, F. R.; Gurewitsch, A. M.; Langmuir, R. V.; Pollock, H. C., "Radiation from Electrons in a Synchrotron", (1947) Physical Review, vol. 71, Issue 11, pp. 829-830

[13] Korchakov, A. A. & Syrovatskii, S. I., 1962, Soviet Astronomy 5, 678.

[14] H. Krawczynski, A. Garson, Q. Guo, et al., "Scientific prospects for hard X-ray polarimetry," Astroparticle Physics, 34 (2011), 550.

[15] Gluckstern, R. L. and Hull, M. H.: 1953, Phys. Rev. 90 (6), 1030.

[16] Gluckstern, R. L. et al., 1953, Phys. Rev. 90 (6), 1026.

[17] Yu. P. Ochelkov, V. V. Usov, "Curvature radiation of relativistic particles in the magnetosphere of pulsars", Astrophysics and Space Science May 1980 (II), Volume 69, Issue 2, pp 439-460

[18] Janusz Gil, Yuri Lyubarsky, George I. Melikidze, "Curvature Radiation in Pulsar Magnetospheric Plasma", The Astrophysical Journal, 600:872-882, 2004 January 10

[19] Jerrold T. Bushberg, J. Anthony Seibert, "The Essential Physics of Medical Imaging," Third edition,

[20] Evans, R. D. 1955, "The atomic nucleus", New York: McGraw-Hill

[21] Remillard, R. A., McClintock, J. E. 2006, ARA&A, 44, 49

[22] Alice K Harding and Dong Lai, "Physics of strongly magnetized neutron stars," Rep. Prog. Phys. 69 (2006) 2631-2708

[23] Stark, R. F., Connors, P. A. 1977, Nature, 266, 429

[24] Connors, P. A., Piran, T., Stark, R. F. 1980, ApJ, 235, 224

[25] Connors, P. A., Stark, R. F. 1980, Nature, 269, 128

[26] Schnittman, J. D., Krolik, J. H. 2009, ApJ, 701, 1175

[27] Schnittman, J. D., Krolik, J. H. 2010, ApJ, 712, 908

[28] Dean, A. J., Clark, D. J., Stephen, J. B. & et al., 2008, Science 321, 1183.

[29] Dyks, J., Harding, A., Rudak, B. 2004, ApJ 606, 1125.

[30] Baring, M. G., Harding, A. K., 2007, Astrophysics and Space Science 308, 109.

[31] Forot, M., Laurent, P., Grenier, I. A. et al., 2008, ApJ 688, L29L32.

[32] Truemper, J., Pietsch, W., Reppin, C., Voges, W., Staubert, R., Kendziorra, E. 1978, ApJ 219, L105.

[33] Staubert, R., Shakura, N., Postnov, K., et al., 2007, A&A 465, 25.

[34] Coburn, W., Heindl, W., Rothschild, R., Gruber, D., Kreykenbohm, I. et al., 2002, ApJ 580, 394.

[35] Semionova, L., Leahy, D. Paez, J. 2010, RAA 10, 1023.

[36] Poutanen, J., 1994, ApJS 92, 607.

[37] McNamara, A. L., Kuncic, Z., Wu, K., 2009, MNRAS 395, 1507.

[38] Zhang, H., Bottcher, M., 2013, ApJ 774, 18.

[39] Marscher, A. P., Jorstad, S. G., DArcangelo, F. D., Smith, P. S., Williams, G. G., Larionov, V. M. et.al., 2008, Nature 452, 966.

[40] Reynoso EM, Hughes JP, Moffett DA, 2013, AJ145, 104

[41] Velusamy, T., 1985, MNRAS, 212, 359.

[42] Bykov, A., Uvarov, Y., Bloemen, J., den Herder, J., Kaastra, J., 2009, MNRAS 399, 1119.

[43] The Pierre Auger Collaboration, 2007, "Correlation of the highest-energy cosmic rays with nearby extragalactic objects," Science 318, 938943

[44] H. L. Marshall, D. E. Harris, J. P. Grimes, J. J. Drake, A. Fruscione, M. Juda, R. P. Kraft, S. Mathur, S. S. Murray, P. M. Ogle, D. O. Pease, D. A. Schwartz, A. L. Siemiginowska, S. D. Vrtilek, and B. J. Wargelin, 2001, "Structure of the X-Ray Emission from the Jet of 3C 273," ApJ 549, pp. L167LL171.

[45] Costa, Enrico, et al., 2010, "POLARIX: a pathfinder mission of X-ray polarimetry.", Experimental Astronomy 28.2-3 (2010): 137-183.

[46] M. C. Begelman and C. F. McKee, 1983, "Compton heated winds and coronae above accretion disks. II Radiative transfer and observable consequences," ApJ 271, pp. 89-112

[47] Beilicke, M., M. G. Baring, S. Barthelmy, W. R. Binns, J. Buckley, R. Cowsik, P. Dowkontt, A. Garson, and Q. Guo. 2011, "Design and tests of the hard x-ray polarimeter X-Calibur," Proc. SPIE 8145, UV, X-Ray, and Gamma-Ray Space Instrumentation for Astronomy XVII

[48] Weisskopf, M. C., Silver, E. H., Kestenbaum, H. L., Long, K. S., & Novick, R. 1978, ApJ, 220, L117

[49] Novick, R. "Stellar and solar X-ray polarimetry," Space Science Reviews 18.3 (1975): 389-408.

[50] Silver, E. H., Weisskopf, M. C., Kestenbaum, H. L., Long, K. S., Novick, R., Wolff, R. S. 1979, ApJ, 232, 248

[51] J. P. Hughes et al., 1984 ApJ., 280, 255-258

[52] Roques, J.P., Schanne, S., von Kienlin, A., et al., 2003, A&A, 411, L91

[53] Winkler, C., et al., "The INTEGRAL mission," Astronomy and Astrophysics-Les Ulis 411.1 (2003): L1.

[54] Vedrenne, G., Roques, J. P., Schonfelder, V., et al., 2003, A&A, 411, L63

[55] Lund, N., Brandt, S., Budtz-Jorgensen, C., et al., 2003, A&A, 411,

[56] Ubertini, P., Lebrun, F., Di Cocco, G., et al., 2003, A&A, 411, L131

[57] D. Yonetoku, T. Murakami, S. Gunji, T. Mihara, T. Sakashita et al., 2010, "Gamma-Ray Burst Polarimeter-GAP-aboard the Small Solar Power Sail Demonstrator IKAROS," arXiv:1010.5305

[58] Tadayuki Takahashi, Kazuhisa Mitsuda, Richard Kelley et al., "The ASTRO-H X-ray Observatory," Proc. SPIE 8443, Space Telescopes and Instrumentation 2012

[59] H. Tajima. et al.,"Soft Gamma-ray Detector for the ASTRO-H Mission", Proc. SPIE 7732, pp. 773216- 773216-17 (2010)

[60] H. Tajima, T. Mitani, T. Tanaka, H. Nakamua, T. Nakamoto, K. Nakazawa, T. Takahashi, Y. Fukazawa, T. Kamae, M. Kokubun, G. Madejski, D. Marlow, M. Nomachi, E. do Couto e Silva, "Gamma-ray polarimetry with Compton Telescope," Proc. SPIE,5488, pp. 561-571 (2004)

[61] Dean, A. J.,Clark, D. J.,Stephen, J. B., et al., 2008, Science, 321, 1183

[62] D. Yonetoku et al., Ap. J. 743 (2011) L30.

[63] D. Yonetoku et al., Ap. J. Lett. 758 (2012) L1.

[64] Takahashi, T., Kelley, R., Mitsuda, K., et al., "The NeXT Mission, Space Telescopes and Instrumentation 2008: Ultraviolet to Gamma Ray," Edited by Turner, Martin J. L.; Flanagan, Kathryn A. Proceedings of the SPIE, Volume 7011, pp. 70110O-70110O-14, 2008.

[65] Mark Pearce, Hans-Gustav Floren et al., 2012 IEEE Nuclear Science Symposium Proceedings, Page(s): 1885 - 1892

[66] M. Jackson, on behalf of the PoGOLite collaboration, 2008, "Balloon-borne hard X-ray astronomy with PoGOLite: Opening a new window on the universe," Mem. S.A.It. Vol., 1, arXiv:1304.7372

[67] Boggs, S. et al., 2006, arXiv:astro-ph/0608532

[68] Black, J. K., Deines-Jones, P., Hill, J. E., et al., 2010, SPIE, 7732, 25.

[69] W. Baumgartner, T. Strohmayer et al., 2012, Proc. SPIE Vol. 8443

[70] P. Soffitta, X. Barcons et al., 2013, "XIPE: the X-ray Imaging Polarimetry Explorer," Experimental Astronomy, Volume 36, 523-567

[71] Qingzhen Guo, Matthias Beilicke, Alfred Garson, Fabian Kislat, David Fleming, Henric Krawczynski, 2013, "Optimization of the Design of the Hard X-ray Polarimeter X-Calibur", Astroparticle Physics, 41, 63-72.

[72] http://infocus.gsfc.nasa.gov/

[73] Ogasaka, Y., Tueller, J., Yamashita, K., et al., 2005, SPIE, 5900, 217

[74] Ramsey, B. D., Alexander, C. D., Apple, J. A., et al., 2002, ApJ, 568, 432

[75] Harrison, F. A., Christensen, F. E., Craig, W., et al., 2005, Experimental Astronomy, 20, 131

[76] Harrison, F. A., Boggs, S., Christensen, F., et al., 2010, SPIE 7732, 21

[77] R. Blanford et al., Proc. IEEE Nucl. Sci. Symp., Portland, USA (2003).

[78] McConnell, M. L., Angelini, L., Baring, M. G., et al., 2009a, AIP Conf. Proc., 1133, 64

[79] McConnell, M. L., Bancroft, C., Bloser, P. F., Connor, T., Legere, J., Ryan, J. M. 2009b, SPIE, 7435, 13

[80] Krawczynski, H. et al., Proc. IEEE, [arXiv:0812.1809].

[81] Sanchez Almeida, J., Martinez Pillet, 1993, "Polarizing properties of grazing-incidence x-ray mirrors comment," Applied Optics, 32, 4231

[82] J. Katsutaa, T. Mizuno, Y. Ogasaka, et al., 2009, "Evaluation of polarization characteristics of multilayer mirror for hard X-ray observation of astrophysical objects," Nuclear Instruments and Methods in Physics Research Section A, 603, 393.

[83] Weisskopf, M. C., et al., 2006, "X-Ray Polarimetry and Its Potential Use for Understanding Neutron Stars," in Neutron Stars and Pulsars, Astrophysics and Space Science Library, 357, p. 589 2009 [astroph/0611483]

[84] Agostinelli, S., Allison, J., Amako, K., et al., 2003, NIMA, 506, 250

[85] S. Chauvie, S. Guatelli, V. Ivanchenko, F. Longo, A. Mantero, B. Mascialino, P. Nieminen, L. Pandola, S. Parlati, L. Peralta, M. G. Pia, M. Piergentili, P. Rodrigues, S. Saliceti, A. Trindade, "Geant4 Low Energy Electromagnetic Physics," Nuclear Science Symposium Conference Record, 2004 IEEE, Page(s): 1881 - 1885 Vol. 3

[86] Tueller, J., Baumgartner, W. H., Markwardt, C. B., et al., 2010, ApJS, 186, 378

[87] Berger, M. J., Hubbell, J. H., Seltzer, S. M., Chang, J., Coursey, J. S., Sukumar, R., Zuck, D. S. 2010, "XCOM: Photon Cross Sections Database"

[88] Ajello, M., Greiner, J., Sato, G., et al., "Cosmic x-ray background and earth albedo spectra with swift bat," ApJ 689, 666677 (2008).

[89] Mizuno, T., Kamae, T., Godfrey, G., et al., "Cosmic-ray background flux model based on a gamma-ray large area space telescope balloon flight engineering model," ApJ 614, 11131123 (2004).

[90] A. Zoglauer, R. Andritschke, F. Schopper, "MEGAlib-the Medium Energy Gamma-ray Astronomy Library," New Astronomy Reviews, vol. 50, no. 7-8, pp. 629-632, 2006

[91] Parsons, A., Barthelmy, S., Bartlett, L., et al., "CdZnTe background measurements at balloon altitudes with PoRTIA," NIMPA 516, 80-95 (2004)

[92] A. Garson III, H. Krawczynski, G. Weidenspointner, E.I. Novikova, J. Grindlay, J. Hong, I.V. Jung, 2006, "CZT in Space Based Hard X-ray Astronomy," arXiv:astro-ph/0610049

[93] K. Slavis, P. Dowkontt, F. Duttweiler, J. Epstein, P. Hink, G. Huszar, P. Leblanc, J. Matteson, R. Skelton, and E. Stephan, "High altitude balloon flight of CdZnTe detectors for high energy X-ray astronomy," EUV, X-ray, and Gamma-ray Instrumentation for Astronomy IX, O. H. W. Siegmund and M. Gummin, eds., Proc. SPIE 3445, p. 169-183, 1998.

[94] K. Slavis, P. Dowkontt, F. Duttweiler, J. Epstein, P. Hink, G. Huszar, P. Leblanc, J. Matteson, R. Skelton, and E. Stephan, "High altitude balloon flight of CdZnTe detectors for high energy X-ray astronomy part ii," EUV, X-ray, and Gamma-ray Instrumentation for Astronomy X, O. H. W. Siegmund and K. A.Flanagan, eds., Proc. SPIE 3765, p. 397-406, 1999

[95] S. Tashenov, A. Khaplanov, B. Cederwall, and K.U. Scha ssburger, Nucl. Instrum. Methods Phys. Res. Sect. A 600, 599 (2009).

[96] S. Tashenov, T. B ack, R. Barday, B. Cederwall, J. Enders, A. Khaplanov, Yu. Poltoratska, K. U. Schassburger, and A. Surzhykov, Phys. Rev. Lett. 107, 173201 (2011).

[97] F.A. Harrison, S. Boggs, F. Christensenand et al., "TheNuclearSpectroscopicTelescopeArray(NuSTAR)", SPIE 7732, 21(2010)

[98] R. Willingale, et al., 2001, "New light on the X-ray spectrum of the Crab Nebula", A&A 365, L212-L217 (2001)

[99] De Geronimo, G., O'Connor, P., Beuttenmuller, R. H., et al., 2003, "Development of a high" rate high resolution detector for exafs experiments", IEEE Transactions on Nuclear Science, 50, 885.

[100] Vernon, E., Ackley, K., de Geronimo, G., et al., 2010, "ASIC for High Rate 3D Position Sensitive Detectors", IEEE Transactions on Nuclear Science, 57, 1536.

[101] De Geronimo, G., Vernon, E., Ackley, K., et al., 2008, "Readout ASIC for 3D Position Sensitive Detectors", IEEE Transactions on Nuclear Science, 55, 1593.

[102] Muleri, F. et al., Nucl.Instrum.Meth. A584 (2008) 149-159 arXiv:0709.4623 [astro-ph]

[103] Marscher, A. P., et al., 2008, Nature, 452, 966

[104] Abdo, A. A., Ackermann, M., Ajello, M., et al., 2010, Nature, 463, 919

[105] Henric Krawczynski, Lorella Angelini, Matthew Baring et al., 2013, "White Paper for Blazar Observations with a GEMS-like X-ray Polarimetry Mission", arXiv:1303.7158

[106] Celotti, A, Matt, G. 1994, MNRAS, 268, 451

[107] Krawczynski, H. 2012, ApJ, 744, 30

[108] M. Boettcher, A. Reimer, K. Sweeney and A. Prakash, 2013, "Leptonic and Hadronic Modeling of Fermi-Detected Blazars," arXiv:1304.0605

[109] Boettcher, M., 2012, "Relativistic Jets of Active Galactic Nuclei," Wiley-VCH, Berlin, Eds. M. Bottcher, D. Harris, H. Krawczynski, Chapter 2

[110] Remillard, R. A., 1999, in Proc. of Frascati Workshop 1997, astro-ph 9805224

[111] Barthelmy et al., 2005, SSRv 120, 143

[112] Gehrels et al., 2004, ApJ 611, 1005

[113] Krimm et al., 2013, ApJSS 209, 14

[114] Tosti, G., Fiorucci, M., Luciani, M., 1998, A&A, 339, 41

[115] Angel, J. R. P., Stockman, H. S. 1980, ARAA, 8, 321

[116] Marco Sorcia, Erika Bentez et al., 2013, "Long-term optical polarization variability of the TeV blazar 1es 1959+650," ApJS 206

[117] Tania P. Dominici, Zulema Abraham et al., 2008, "Optical polarization variability in TeV blazars," Workshop on Blazar Variability across the Electromagnetic Spectrum

[118] http://www.asdc.asi.it/bzcat/

[119] http://tevcat.uchicago.edu/

[120] http://swift.gsfc.nasa.gov/results/bs70mon/

[121] http://glastweb.pg.infn.it/blazar/

[122] A. A. Abdo, M. Ackermann, M. Ajello, M. Axelsson, L. Baldini, J. Ballet, G. Barbiellini, et al., 2009, "The Spectral Energy Distribution of Fermi bright blazars," arXiv:0912.2040

[123] Larionov, V. M., Konstantinova, T. S., Blinov, D. A., 2009, "Optical unprecedented high brightness level of blazar PKS 1510-08," The Astronomer's Telegram, 2045

[124] Fan, J H, Cheng, K S; Zhang, L, 1999, "Polarization and beaming effect for BL Lacertae objects-II," astro-ph/9910538

[125] Scarpa, R., Falomo, R. 1997, A& A, 325, 109

[126] Visvanathan, N., 1967, "Polarization Observations in the Radio Galaxy 3C 371 and the X-Ray Source CYG X-2," Astrophysical Journal, vol. 150, p.L149